

Thermodynamically consistent phase-field modeling and numerical simulation for two-phase fluid-solid dynamics

Cedric Riethmüller^{a,*}, Lars von Wolff^a, Dominik Göddeke^a, Christian Rohde^a

^a Institute of Applied Analysis and Numerical Simulation & Stuttgart Center for Simulation Science (SC SimTech),
University of Stuttgart, Germany
(Emails: {cedric.riethmueller, dominik.goeddeke, christian.rohde, lars.von-wolff}@ians.uni-stuttgart.de)

Abstract

We introduce a coupled Cahn-Hilliard Navier-Stokes model that governs the two-phase dynamics of a system that consists of a fluid and a solid phase and prove its thermodynamic consistency. Moreover, we present an associated fully-discrete numerical method that relies on a continuous finite element approach and a semi-implicit time-stepping method. As the main theoretical result we show that the fully-discrete method satisfies a discrete analog of the free energy dissipation inequality.

Numerical experiments confirm the theoretical findings and show the applicability of the method for realistic settings including an extension to chemically reacting flow. In this context, we provide a preprocessing strategy that enables computing fluid flow in complex geometries given a sharp-interface formulation of the initial phase distribution. Moreover, we briefly introduce different solution strategies for the novel discretization based on the monolithic and partitioned solution paradigms and assess these in a comparative study.

Keywords: Phase-field model, Cahn-Hilliard, Navier-Stokes, Thermodynamic consistency, Solution strategies, Precipitation/dissolution

1. Introduction

We introduce a phase-field model for fluid-solid single-phase flow comprising the Navier-Stokes equations for evaluating the flow field and the Cahn-Hilliard evolution for calculating the interfacial dynamics of the fluid and the solid phase. The model's intrinsic complexity lies in its coupled multiphysics nature along with the nonlinearity of both subproblems and its nonconvexity. In terms of modeling aspects, the model is closely related to the Abels-Garcke-Grün (AGG) phase-field model for two-phase incompressible flow [1].

The two-phase model we present in this work can be derived from the ternary δ -2f1s-model introduced in [2, 3]. Further models have been derived from the latter including models for precipitation and dissolution [4, 5] that also feature a solid and a fluid phase but in addition take reactions into account and hence solve for an ion concentration. While for the continuous ternary model and thus also for these derived ones, the proof of thermodynamic consistency is rather straightforward, there is no discretization proposed yet that allows for the discrete counterpart to hold.

A central focus of this work is on considerations related to thermodynamic consistency. Firstly, we prove the latter for the governing two-phase model. Moreover, we establish a thermodynamically consistent discretization, enabling us to obtain stable numerical methods for the model. The literature for unconditionally gradient-stable schemes for Cahn-Hilliard Navier-Stokes models is quite rich, especially in the context of two-phase incompressible flows [6, 7, 8, 9, 10, 11, 12]. Other representatives of this class of schemes are established for models governing moving contact line problems [13], a quasi-incompressible form (with

*Corresponding author

a non-solenoidal velocity field) [14], variable density two-phase incompressible surface flow [15], dynamic boundary conditions [16], reactive multi-species flow [17], and three-phase flow [18].

Furthermore, we provide a strategy to use our model to compute fluid flow in complex geometries given a sharp-interface formulation of the initial phase distribution. Here, the proposed ansatz works as a preprocessing step and hence does not require changes to the model formulation but rather to the parameter configuration. A pivotal point is that the fluid-solid interface is only moving due to geometric effects and thus almost static. This is in contrast to Cahn-Hilliard Navier-Stokes models developed in the diffuse-domain context [19, 20] which on the one hand introduce a second phase-field parameter for the domain boundary but on the other hand intrinsically satisfy the staticity requirement. In this context, we also refer to Chapter 4 of [3]. There also exist other in some sense contrary approaches that allow for changes in the (solid) structure as for example in the field of shape and topology optimization. Here, the underlying mathematical task is to solve a constrained optimization problem in order to minimize a structure-related objective functional subject to PDE constraints. Besides convolution-thresholding methods [21, 22], phase-field methods are employed to solve this task, e.g. for fluid flow [23].

Moreover, we briefly assess different solution strategies for the novel discretization based on the monolithic and partitioned solution paradigms comprising a feasible preconditioning strategy for the latter case. Efficient solution approaches for Cahn-Hilliard Navier-Stokes models with a focus on preconditioned iterative solvers are investigated in [24] for the monolithic case and in [25, 26] for the partitioned case.

The outline of this work is as follows. In Section 2 we start by introducing the governing two-phase model. We prove its thermodynamic consistency in Section 3, followed by a derivation of the (fully) discretized system in Section 4. As the main theoretical result, we provide with Theorem 4.1 a discrete free energy dissipation inequality yielding the thermodynamic consistency of the proposed discrete system. In Section 5 we establish numerical solution strategies based on the monolithic and partitioned paradigms, along with some notes on preconditioning techniques for the latter case. We further present a flexible preprocessing strategy for generating initial conditions for the phase-field variable taking parametrized sharp-interface descriptions as input in Section 6. Lastly, Section 7 is devoted to numerical experiments that assess the modeling capabilities, thermodynamic consistency, and numerical solution strategies introduced before. In particular, in Section 7.3 we extend the numerical method to account for precipitation/dissolution effects at the interface between the solid and the liquid phase. We end with concluding remarks in Section 8.

2. Formulation of a model for two-phase fluid-solid dynamics

In this section we introduce the governing diffuse-interface model for the interfacial dynamics of a fluid and a solid phase. It consists of a coupled Cahn-Hilliard Navier-Stokes system and accounts for the hydromechanics of the fluid phase coupled to the phase-field evolution of the diffuse fluid-solid interface. On the one hand, it can be understood as an adaption of the Cahn-Hilliard Navier-Stokes model from [1] that describes the motion of two fluid phases. On the other hand, it turns out to be a consequence of the model from [2] which in addition accounts for reactive transport of ions and the associated precipitation/dissolution processes at the fluid-solid interface.

Let $\Omega \subset \mathbb{R}^\nu$, $\nu \in \{2, 3\}$, be a bounded domain with Lipschitz boundary $\partial\Omega$ and $(0, T]$ a time interval with final time $0 < T < \infty$. As the phase-field variable ϕ we consider the volume fraction of the fluid phase, that is, $\phi = 1$ in the fluid phase and $\phi = 0$ in the solid phase. In a thin layer around the fluid-solid interface, called the diffuse transition zone, ϕ runs smoothly between 0 and 1. The two-phase model reads

$$\begin{aligned} \nabla \cdot (\tilde{\phi}_f \mathbf{v}) &= 0, \\ \partial_t (\tilde{\phi}_f \mathbf{v}) + \nabla \cdot ((\rho_f \mathbf{v} + \mathbf{J}_f) \otimes \mathbf{v}) &= -\tilde{\phi}_f \nabla p + \nabla \cdot (2\gamma \nabla^s \mathbf{v}) - \rho d(\tilde{\phi}_f, \varepsilon) \mathbf{v} + \tilde{\mathbf{S}}, \\ \partial_t \phi + \nabla \cdot (\phi \mathbf{v} + \mathbf{J}) &= 0, \\ \mu &= \frac{W'_{dw}(\phi)}{\varepsilon} - \varepsilon \Delta \phi \end{aligned} \quad \text{in } \Omega \times (0, T). \quad (1)$$

In (1), the unknowns are the pressure $p: (\mathbf{x}, t) \mapsto \mathbb{R}$, the velocity $\mathbf{v}: (\mathbf{x}, t) \mapsto \mathbb{R}^\nu$, the phase-field variable $\phi: (\mathbf{x}, t) \mapsto [0, 1]$ and the chemical potential $\mu: (\mathbf{x}, t) \mapsto \mathbb{R}$.

The fluid fraction $\tilde{\phi}_f$ is defined for a small but fixed regularization parameter $\delta > 0$ by

$$\tilde{\phi}_f = 2\delta + (1 - 2\delta)\phi. \quad (2)$$

We denote the density of the fluid phase by ρ . Furthermore,

$$\rho_f = \rho\phi \quad \text{and} \quad \tilde{\rho}_f = \rho_f + \rho\delta. \quad (3)$$

We introduce

$$\mathbf{J} = -M\varepsilon\nabla\mu \quad \text{and} \quad \mathbf{J}_f = \rho\mathbf{J} \quad (4)$$

as the Cahn-Hilliard fluxes with constant state-independent mobility M .

As is usual for phase-field models we introduce a parameter $\varepsilon > 0$ such that the width of the diffuse transition zone is of order ε . The function $W_{\text{dw}}(\phi)$ is a double-well potential taking minimal values in the pure phases ($\phi = 0$ and $\phi = 1$).

In the momentum equations (1)₂, the constant $\gamma > 0$ denotes the state-independent viscosity, $d(\tilde{\phi}_f, \varepsilon)$ accounts for velocity dissipation and $\tilde{\mathbf{S}}$ models surface tension effects, see equation (6) for the precise definition.

We augment (1) with initial and boundary conditions given by

$$\mathbf{v}(\cdot, 0) = \mathbf{v}_0, \phi(\cdot, 0) = \phi_0 \text{ in } \Omega, \quad \mathbf{v} = \mathbf{0}, \nabla\phi \cdot \mathbf{n} = 0, \nabla\mu \cdot \mathbf{n} = 0 \text{ on } \partial\Omega. \quad (5)$$

Here, $\mathbf{v}_0 : \Omega \rightarrow \mathbb{R}^{\nu}$ and $\phi_0 : \Omega \rightarrow [0, 1]$ denote the given initial velocity and phase field, and $\mathbf{n} \in \mathbb{R}^{\nu}$ denotes the outer normal unit vector on $\partial\Omega$.

In the following remark we discuss the key modeling aspects related to (1).

Remark 2.1 (Modeling aspects). (i) We follow the seminal modeling approach for the incompressible flow of two fluid phases as introduced in [1]. In particular, for the incompressibility equation (1)₁, we follow the idea of volume averaging presented in [1] which in the given setting leads to $\tilde{\phi}_f \mathbf{v}$ being divergence free, replacing the usual incompressibility constraint on \mathbf{v} alone.

(ii) δ -regularization: As smooth phase-field parameter ϕ we consider the volume fraction of the fluid phase. Hence, it would be desirable to ensure that for all $\mathbf{x} \in \Omega$ and $t \in [0, T]$ the range restriction $\phi(\mathbf{x}, t) \in [0, 1]$ is satisfied. However, the Cahn-Hilliard evolution that models the phase-field dynamics is known to not fulfill a priori such a maximum principle. As a means of remediation, we employ an unbounded potential function of the general form

$$W_{\text{dw}}(\phi) = \phi^2(1 - \phi)^2 + \ell(\phi) + \ell(1 - \phi)$$

with the classical quartic term and a limiter function $\ell(\phi)$ that diverges at $\phi = -\delta$ for some small $\delta > 0$. Thus, $W_{\text{dw}}(\phi)$ diverges at $\phi = -\delta$ and $\phi = 1 + \delta$ and by establishing an energy estimate the relaxed constraint $\phi(\mathbf{x}, t) \in (-\delta, 1 + \delta)$ is satisfied.

Using δ from the definition of the double-well potential in equations (2) and (3), we directly obtain that for $\phi > -\delta$ the quantities $\tilde{\phi}_f$ and $\tilde{\rho}_f$ are positive. In this way, the δ -modification prevents the two-phase model (1) from degeneration.

Note that in the limit $\delta \rightarrow 0$ the double-well function $W_{\text{dw}}(\phi)$ converges point-wise to a potential of double-obstacle type. There exists extensive analysis for the Cahn-Hilliard equation with double-obstacle potential, cf. e.g. [27]. For numerical reasons, however, we refrain from following this ansatz as it results in a model comprising variational inequalities.

(iii) The solid phase is assumed to be immobile. By rewriting the pressure-like term in the momentum equations (1)₂ as

$$-\tilde{\phi}_f \nabla p = -\nabla \left(\tilde{\phi}_f p \right) + p \nabla \tilde{\phi}_f$$

it becomes apparent that the latter can be a source (or sink) for momentum. As $\nabla\phi$ is perpendicular to the fluid-solid interface, the second term acts as a normal force between the two phases.

In order to achieve thermodynamic consistency below, we follow the approach of adding a flux term in the momentum equations, cf. [1], and generalize it to the case of a solid phase present in the model, yielding the contribution $\nabla \cdot (\mathbf{J}_f \otimes \mathbf{v})$.

Concerning the drag term $d(\tilde{\phi}_f, \varepsilon)$, the function $d(\cdot, \varepsilon)$ can be any smooth, decreasing function satisfying $d(1, \varepsilon) = 0$ and $d(0, \varepsilon) = d_0$ with positive constant d_0 independent of ε . This term ensures that for the solid phase the velocity is small. In practice, we choose $d(\tilde{\phi}_f, \varepsilon) = d_0(1 - \tilde{\phi}_f)^2$. Together with the assumption of a constant viscosity γ independent of ϕ , we are able to ensure a no-slip condition between the solid and fluid phase by choosing the constant d_0 sufficiently large; see also Remark 3.3 in [3].

Lastly, the (effective) surface tension is given as

$$\tilde{\mathbf{S}} = 2\delta\sigma(1 - \phi)\nabla\mu \quad (6)$$

with the (constant) surface tension coefficient $\sigma > 0$ between the two phases. This term is indispensable for the (proof of) thermodynamic consistency, but has little influence on the global solution as it is scaled with δ .

- (iv) The classical formulation of the Cahn-Hilliard equation leads to fourth order operators. To enable a proper notion of a weak solution we split the equation of fourth order in space into the two equations (1)_{3,4} of second order introducing the chemical potential μ . The coupling to the Navier-Stokes equations (1)_{1,2} is due to the advection of the fluid phase only. Note again that the solid phase is not advected.
- (v) The boundary conditions in (5) provide a simple setting. For the theoretical part we make no attempt to account for inflow/outflow conditions or more advanced concepts like the enforcement of dynamic contact angles.

3. Thermodynamic consistency

In this section we show in Theorem 3.1 that smooth solutions of (1) dissipate an appropriate free energy functional. The results are the basis for the corresponding discrete result on energy dissipation in Section 4.

Consider the free energy functional

$$F[\phi(\cdot, t), \nabla\phi(\cdot, t), \mathbf{v}(\cdot, t)] = \int_{\Omega} \frac{1}{2} \tilde{\rho}_f(\mathbf{x}, t) |\mathbf{v}(\mathbf{x}, t)|^2 + f(\phi(\mathbf{x}, t), \nabla\phi(\mathbf{x}, t)) \, d\mathbf{x}. \quad (7)$$

It comprises the kinetic energy of the fluid phase and the potential energy contribution as the Ginzburg-Landau energy

$$f(\varphi, \boldsymbol{\xi}) = \sigma \left(\frac{W_{\text{dw}}(\varphi)}{\varepsilon} + \frac{\varepsilon}{2} |\boldsymbol{\xi}|^2 \right).$$

We readily deduce:

Theorem 3.1. *Let $(p, \mathbf{v}, \phi, \mu)$ be a smooth solution of the two-phase model (1) which satisfies the boundary conditions from (5).*

Then, (\mathbf{v}, ϕ, μ) fulfills the free energy dissipation inequality

$$\begin{aligned} \frac{d}{dt} F[\phi(\cdot, t), \nabla\phi(\cdot, t), \mathbf{v}(\cdot, t)] \\ = \int_{\Omega} -2\gamma \nabla^s \mathbf{v}(\mathbf{x}, t) : \nabla \mathbf{v}(\mathbf{x}, t) - \rho d(\tilde{\phi}_f(\mathbf{x}, t), \varepsilon) |\mathbf{v}(\mathbf{x}, t)|^2 - \sigma M \varepsilon |\nabla\mu(\mathbf{x}, t)|^2 \, d\mathbf{x} \\ \leq 0 \end{aligned} \quad (8)$$

for all $t \in (0, T]$.

Proof. By basic vector calculus (cf. (A.1) in Lemma A.1 in the appendix) and the boundary condition on \mathbf{v} in (5) we deduce after partial integration

$$\begin{aligned} \int_{\Omega} \mathbf{v} \cdot \left(\nabla \cdot ((\rho_f \mathbf{v} + \mathbf{J}_f) \otimes \mathbf{v}) \right) d\mathbf{x} &= \int_{\Omega} \mathbf{v} \cdot \left(\nabla \cdot (\rho_f \mathbf{v} + \mathbf{J}_f) \mathbf{v} + ((\rho_f \mathbf{v} + \mathbf{J}_f) \cdot \nabla) \mathbf{v} \right) d\mathbf{x} \\ &= \int_{\Omega} |\mathbf{v}|^2 \nabla \cdot (\rho_f \mathbf{v} + \mathbf{J}_f) + \frac{1}{2} ((\rho_f \mathbf{v} + \mathbf{J}_f) \cdot \nabla) |\mathbf{v}|^2 d\mathbf{x} \\ &= \int_{\Omega} \frac{1}{2} |\mathbf{v}|^2 \nabla \cdot (\rho_f \mathbf{v} + \mathbf{J}_f) d\mathbf{x}. \end{aligned}$$

Using the definitions of $\tilde{\rho}_f$, ρ_f from (3) and \mathbf{J}_f from (4), we obtain with (1)₃ the evolution equation

$$\partial_t \tilde{\rho}_f = \partial_t (\rho \phi + \rho \delta) = \rho \partial_t \phi = -\nabla \cdot (\rho \phi \mathbf{v} + \rho \mathbf{J}) = -\nabla \cdot (\rho_f \mathbf{v} + \mathbf{J}_f).$$

Together with (1)₁ and (1)₂ the time derivative of the kinetic energy (of the fluid phase) can then be calculated as

$$\begin{aligned} \frac{d}{dt} \int_{\Omega} \frac{1}{2} \tilde{\rho}_f |\mathbf{v}|^2 d\mathbf{x} &= \int_{\Omega} \mathbf{v} \cdot \partial_t (\tilde{\rho}_f \mathbf{v}) - \frac{1}{2} |\mathbf{v}|^2 \partial_t \tilde{\rho}_f d\mathbf{x} \\ &= \int_{\Omega} -\mathbf{v} \cdot \left(\nabla \cdot ((\rho_f \mathbf{v} + \mathbf{J}_f) \otimes \mathbf{v}) \right) - \tilde{\rho}_f \mathbf{v} \cdot \nabla p + \mathbf{v} \cdot (\nabla \cdot (2\gamma \nabla^s \mathbf{v})) \\ &\quad - \rho d(\tilde{\phi}_f, \varepsilon) |\mathbf{v}|^2 + \tilde{\mathbf{S}} \cdot \mathbf{v} + \frac{1}{2} |\mathbf{v}|^2 \nabla \cdot (\rho_f \mathbf{v} + \mathbf{J}_f) d\mathbf{x} \\ &= \int_{\Omega} \mathbf{v} \cdot (\nabla \cdot (2\gamma \nabla^s \mathbf{v})) - \rho d(\tilde{\phi}_f, \varepsilon) |\mathbf{v}|^2 + \tilde{\mathbf{S}} \cdot \mathbf{v} d\mathbf{x} \\ &= \int_{\Omega} -2\gamma \nabla^s \mathbf{v} : \nabla \mathbf{v} - \rho d(\tilde{\phi}_f, \varepsilon) |\mathbf{v}|^2 + \tilde{\mathbf{S}} \cdot \mathbf{v} d\mathbf{x}, \end{aligned}$$

using again (5). Next, for the time derivative of the Ginzburg-Landau free energy f we obtain

$$\begin{aligned} \frac{d}{dt} \int_{\Omega} f(\phi, \nabla \phi) d\mathbf{x} &= \int_{\Omega} \frac{\partial f}{\partial \phi} \partial_t \phi + \frac{\partial f}{\partial \nabla \phi} \partial_t \nabla \phi d\mathbf{x} = \int_{\Omega} \left(\frac{\partial f}{\partial \phi} - \nabla \cdot \frac{\partial f}{\partial \nabla \phi} \right) \partial_t \phi d\mathbf{x} \\ &= \int_{\Omega} \sigma \left(\frac{W'_{\text{dw}}(\phi)}{\varepsilon} - \varepsilon \Delta \phi \right) \partial_t \phi d\mathbf{x} \stackrel{(1)_4}{=} \int_{\Omega} \sigma \mu \partial_t \phi d\mathbf{x} \\ &\stackrel{(1)_3}{=} \int_{\Omega} -\sigma \mu (\nabla \cdot (\phi \mathbf{v} + \mathbf{J})) d\mathbf{x} \\ &= \int_{\Omega} -\sigma \mu \nabla \cdot (\phi \mathbf{v}) d\mathbf{x} + \int_{\Omega} -\sigma \mu \nabla \cdot \mathbf{J} d\mathbf{x}. \end{aligned}$$

By (1)₁ we have

$$0 = \nabla \cdot (\tilde{\phi}_f \mathbf{v}) = \nabla \cdot ((2\delta + (1-2\delta)\phi) \mathbf{v}) = \nabla \cdot (\phi \mathbf{v}) + 2\delta \nabla \cdot ((1-\phi) \mathbf{v}),$$

yielding

$$\begin{aligned} \int_{\Omega} \sigma \mu \nabla \cdot (\phi \mathbf{v}) d\mathbf{x} &= \int_{\Omega} -2\delta \sigma \mu \nabla \cdot ((1-\phi) \mathbf{v}) d\mathbf{x} = \int_{\Omega} 2\delta \sigma (1-\phi) \nabla \mu \cdot \mathbf{v} d\mathbf{x} \\ &= \int_{\Omega} \tilde{\mathbf{S}} \cdot \mathbf{v} d\mathbf{x}. \end{aligned} \tag{9}$$

Hence, we obtain

$$\begin{aligned} \frac{d}{dt} \int_{\Omega} f(\phi, \nabla \phi) d\mathbf{x} &= - \int_{\Omega} \tilde{\mathbf{S}} \cdot \mathbf{v} d\mathbf{x} + \int_{\Omega} -\sigma \mu \nabla \cdot \mathbf{J} d\mathbf{x} \\ &= - \int_{\Omega} \tilde{\mathbf{S}} \cdot \mathbf{v} d\mathbf{x} + \int_{\Omega} -\sigma M \varepsilon |\nabla \mu|^2 d\mathbf{x}. \end{aligned}$$

Thus, for the time derivative of the total free energy functional we have

$$\frac{d}{dt} F[\phi, \nabla \phi, \mathbf{v}] = \int_{\Omega} -2\gamma \nabla^s \mathbf{v} : \nabla \mathbf{v} - \rho d(\tilde{\phi}_f, \varepsilon) |\mathbf{v}|^2 - \sigma M \varepsilon |\nabla \mu|^2 d\mathbf{x},$$

and since $\nabla^s \mathbf{v} : \nabla \mathbf{v} \geq 0$ this concludes the proof. \square

4. An energy-consistent discretization for the fluid-solid system

In this section we present a fully-discrete numerical method to approximate the initial-boundary value problem for the fluid-solid dynamics in (1) with initial and boundary conditions from (5). The method relies on a finite element discretization in space. We employ a specific time-stepping method to ensure the thermodynamic consistency of the fully-discrete approach. This main result on the discretization is given in Theorem 4.1 below.

4.1. Weak formulation and fully-discrete approach

The discretization relies on a slight reformulation of the momentum equations in (1). In fact, using $\rho = \text{const.}$, we can rewrite the Cahn-Hilliard evolution in (1)₃ in terms of the fluid density, i.e.,

$$\partial_t \phi + \nabla \cdot (\phi \mathbf{v} + \mathbf{J}) = 0 \iff \partial_t (\rho \phi + \rho \delta) + \nabla \cdot (\rho \phi \mathbf{v} + \rho \mathbf{J}) = 0 \iff \partial_t \tilde{\rho}_f + \nabla \cdot (\rho_f \mathbf{v} + \mathbf{J}_f) = 0$$

Thus, we have for the inertial operator

$$\begin{aligned} \partial_t (\tilde{\rho}_f \mathbf{v}) + \nabla \cdot ((\rho_f \mathbf{v} + \mathbf{J}_f) \otimes \mathbf{v}) \\ = \tilde{\rho}_f \partial_t \mathbf{v} + \partial_t \tilde{\rho}_f \mathbf{v} + \nabla \cdot (\rho_f \mathbf{v} + \mathbf{J}_f) \mathbf{v} + ((\rho_f \mathbf{v} + \mathbf{J}_f) \cdot \nabla) \mathbf{v} \\ = \tilde{\rho}_f \partial_t \mathbf{v} + ((\rho_f \mathbf{v} + \mathbf{J}_f) \cdot \nabla) \mathbf{v} + [\partial_t \tilde{\rho}_f + \nabla \cdot (\rho_f \mathbf{v} + \mathbf{J}_f)] \mathbf{v} \\ = \tilde{\rho}_f \partial_t \mathbf{v} + ((\rho_f \mathbf{v} + \mathbf{J}_f) \cdot \nabla) \mathbf{v}, \end{aligned}$$

and obtain for (1)₂ the equivalent relation

$$\tilde{\rho}_f \partial_t \mathbf{v} + ((\rho_f \mathbf{v} + \mathbf{J}_f) \cdot \nabla) \mathbf{v} = -\tilde{\phi}_f \nabla p + \nabla \cdot (2\gamma \nabla^s \mathbf{v}) - \rho d(\tilde{\phi}_f, \varepsilon) \mathbf{v} + \tilde{\mathbf{S}}. \quad (10)$$

Based on this form we introduce a weak formulation of the two-phase model.

We use the standard notation for Sobolev spaces, see e.g. [28], and introduce the space of square-integrable functions with zero mean $L_0^2(\Omega) := \{f \in L^2(\Omega) \mid \frac{1}{|\Omega|} \int_{\Omega} f d\mathbf{x} = 0\}$.

The quadruple

$$(p, \mathbf{v}, \phi, \mu) \in L_0^2(\Omega) \times H_0^1(\Omega)^{\nu} \times H^1(\Omega) \times H^1(\Omega) \quad (11)$$

is called a weak solution of the two-phase model (1), with the given initial and boundary data from (5), if the initial conditions in (5) hold a.e. in Ω and if

$$\begin{aligned} 0 &= - \int_{\Omega} \tilde{p} \nabla \cdot (\tilde{\phi}_f \mathbf{v}) d\mathbf{x}, \\ 0 &= \int_{\Omega} \tilde{\rho}_f \partial_t \mathbf{v} \cdot \tilde{\mathbf{v}} d\mathbf{x} + \int_{\Omega} (((\rho_f \mathbf{v} + \mathbf{J}_f) \cdot \nabla) \mathbf{v}) \cdot \tilde{\mathbf{v}} d\mathbf{x} \\ &\quad - \int_{\Omega} p \nabla \cdot (\tilde{\phi}_f \tilde{\mathbf{v}}) d\mathbf{x} + \int_{\Omega} 2\gamma \nabla^s \mathbf{v} : \nabla \tilde{\mathbf{v}} d\mathbf{x} + \int_{\Omega} \rho d(\tilde{\phi}_f, \varepsilon) \mathbf{v} \cdot \tilde{\mathbf{v}} d\mathbf{x} - \int_{\Omega} \tilde{\mathbf{S}} \cdot \tilde{\mathbf{v}} d\mathbf{x}, \\ 0 &= \int_{\Omega} (\partial_t \phi) \tilde{\phi} d\mathbf{x} - \int_{\Omega} (\phi \mathbf{v} + \mathbf{J}) \cdot \nabla \tilde{\phi} d\mathbf{x}, \\ 0 &= \int_{\Omega} \mu \tilde{\mu} d\mathbf{x} - \int_{\Omega} \frac{W'_{\text{dw}}(\phi)}{\varepsilon} \tilde{\mu} d\mathbf{x} - \int_{\Omega} \varepsilon \nabla \phi \cdot \nabla \tilde{\mu} d\mathbf{x} \end{aligned} \quad (12)$$

holds for all $\tilde{p} \in L_0^2(\Omega)$, $\tilde{\mathbf{v}} \in H_0^1(\Omega)^{\nu}$ and $\tilde{\phi}, \tilde{\mu} \in H^1(\Omega)$, and a.e. in $(0, T)$.

Note that the boundary conditions from (5) are encoded in the ansatz spaces. In what follows we assume that there exists a unique weak solution $(p, \mathbf{v}, \phi, \mu) \in L_0^2(\Omega) \times H_0^1(\Omega)^\nu \times H^1(\Omega) \times H^1(\Omega)$ of the two-phase model (1). We conjecture that a rigorous well-posedness analysis for weak solutions can be achieved following e.g. [29, 30].

Before discretizing (12), we make two equivalent reformulations in (12)₂ that are essential for showing thermodynamic consistency afterwards. Firstly, as proposed in [7], we split the convective term as

$$\begin{aligned} & \int_{\Omega} (((\rho_f \mathbf{v} + \mathbf{J}_f) \cdot \nabla) \mathbf{v}) \cdot \tilde{\mathbf{v}} \, d\mathbf{x} \\ & \stackrel{(A.3)}{=} \frac{1}{2} \int_{\Omega} (\rho_f \mathbf{v} + \mathbf{J}_f) \cdot \nabla (\mathbf{v} \cdot \tilde{\mathbf{v}}) \, d\mathbf{x} + \frac{1}{2} \int_{\Omega} (\rho_f \mathbf{v} + \mathbf{J}_f) \cdot ((\nabla \mathbf{v}) \tilde{\mathbf{v}}) \, d\mathbf{x} - \frac{1}{2} \int_{\Omega} (\rho_f \mathbf{v} + \mathbf{J}_f) \cdot ((\nabla \tilde{\mathbf{v}}) \mathbf{v}) \, d\mathbf{x}. \end{aligned}$$

Secondly, for the surface tension term we use (9) and partial integration to obtain

$$\int_{\Omega} \tilde{\mathbf{S}} \cdot \tilde{\mathbf{v}} \, d\mathbf{x} = \int_{\Omega} \sigma \mu \nabla \cdot (\phi \tilde{\mathbf{v}}) \, d\mathbf{x} = - \int_{\Omega} \sigma (\phi \tilde{\mathbf{v}}) \cdot \nabla \mu \, d\mathbf{x}.$$

Mimicking the continuous case, both reformulations are needed to eventually cancel contributions from the convective term in (12)₃.

To introduce our numerical method for weak solutions, we employ a Galerkin finite element method on a conforming triangular mesh \mathcal{T}_h that consists of closed simplices $\{T\}_{T \in \mathcal{T}_h}$ with spatial measures $h_T = \text{diam}(T)$ and $h = \max_{T \in \mathcal{T}_h} h_T$, such that $\overline{\Omega} = \cup_{T \in \mathcal{T}_h} \overline{T}$. As discrete ansatz spaces we choose Lagrange finite element spaces denoted by \mathcal{V}_h^p , \mathcal{V}_h^v and $\mathcal{V}_h^{\text{ch}}$ (for ϕ and μ), respectively with

$$\begin{aligned} \mathcal{V}_h^{\text{ch}} &= \left\{ \eta_h \in C(\overline{\Omega}) \mid \eta_h|_T \in \mathcal{P}^j(T) \text{ for all } T \in \mathcal{T}_h \right\}, \\ \mathcal{V}_h^p &= \left\{ p_h \in C(\overline{\Omega}) \mid p_h|_T \in \mathcal{P}^k(T) \text{ for all } T \in \mathcal{T}_h \right\} \cap L_0^2(\Omega), \\ \mathcal{V}_h^v &= \left\{ \mathbf{v}_h \in C(\overline{\Omega})^\nu \mid \mathbf{v}_h|_T \in (\mathcal{P}^l(T))^\nu \text{ for all } T \in \mathcal{T}_h, \quad \mathbf{v}_h|_{\partial\Omega} = 0 \right\}. \end{aligned} \quad (13)$$

Here, $\mathcal{P}^l(T)$ denotes the set of polynomials of degree at most l on the simplex T . The choice of the Lagrangian finite element spaces is for the sake of definiteness. For our main result in Theorem 4.1 we only require the ansatz spaces to be embedded into the ansatz space $L_0^2(\Omega) \times H_0^1(\Omega)^\nu \times H^1(\Omega) \times H^1(\Omega)$ from (11). Let us also note that polynomial exponents j, k, l do not need to be related to prove Theorem 4.1. For conditions that imply stability for the velocity-pressure pair we refer to [31] and for the specific spaces used in our work to Section 7 below.

In time we divide the temporal domain $[0, T]$ into subintervals $[t^n, t^{n+1}]$ for $n = 0, \dots, N_t - 1$ with $t^{n+1} = t^n + \tau$ for constant time step $\tau = \frac{T}{N_t} > 0$. Given the values for the primary variables $p^n, \mathbf{v}^n, \phi^n$ and μ^n at time t^n , we then search for $p^{n+1}, \mathbf{v}^{n+1}, \phi^{n+1}$ and μ^{n+1} in the corresponding finite element spaces. For the time discretization, we employ a tailor-made semi-implicit Euler method in order to account for thermodynamic consistency. The extension to higher-order in time methods remains an open challenge. For the double-well potential $W_{\text{dw}}(\phi)$ we employ a convex-concave split of the form

$$W_{\text{dw}}(\phi) = W_c(\phi) + W_e(\phi) \quad (14)$$

with convex part $W_c(\phi)$ and concave part $W_e(\phi)$. The convex part is then evaluated implicitly and the concave part explicitly following [32].

With these preparations the fully-discrete method is given as follows. Let $(p^0, \mathbf{v}^0, \phi^0, \mu^0) \in \mathcal{V}_h^p \times \mathcal{V}_h^v \times \mathcal{V}_h^{\text{ch}} \times \mathcal{V}_h^{\text{ch}}$ denote the discrete initial data that are determined from L^2 -projection to the finite element spaces.

We search for $n = 1, \dots, N_t$ the approximates $(p^n, \mathbf{v}^n, \phi^n, \mu^n) \in \mathcal{V}_h^p \times \mathcal{V}_h^v \times \mathcal{V}_h^{\text{ch}} \times \mathcal{V}_h^{\text{ch}}$ such that

$$\begin{aligned}
0 &= - \int_{\Omega} \check{p} \nabla \cdot (\tilde{\phi}_f^{n+1} \mathbf{v}^{n+1}) \, d\mathbf{x}, \\
0 &= \int_{\Omega} \frac{\tilde{\rho}_f^n + \tilde{\rho}_f^{n+1}}{2} \frac{\mathbf{v}^{n+1} - \mathbf{v}^n}{\tau} \cdot \check{\mathbf{v}} \, d\mathbf{x} \\
&\quad + \frac{1}{2} \int_{\Omega} (\rho_f^n \mathbf{v}^{n+1} + \mathbf{J}_f^{n+1}) \cdot \nabla (\mathbf{v}^n \cdot \check{\mathbf{v}}) \, d\mathbf{x} + \frac{1}{2} \int_{\Omega} (\rho_f^n \mathbf{v}^n + \mathbf{J}_f^n) \cdot ((\nabla \mathbf{v}^{n+1}) \check{\mathbf{v}}) \, d\mathbf{x} \\
&\quad - \frac{1}{2} \int_{\Omega} (\rho_f^n \mathbf{v}^n + \mathbf{J}_f^n) \cdot ((\nabla \check{\mathbf{v}}) \mathbf{v}^{n+1}) \, d\mathbf{x} \\
&\quad - \int_{\Omega} p^{n+1} \nabla \cdot (\tilde{\phi}_f^{n+1} \check{\mathbf{v}}) \, d\mathbf{x} + \int_{\Omega} 2\gamma \nabla^s \mathbf{v}^{n+1} : \nabla \check{\mathbf{v}} \, d\mathbf{x} \\
&\quad + \int_{\Omega} \rho d(\tilde{\phi}_f^n, \varepsilon) \mathbf{v}^{n+1} \cdot \check{\mathbf{v}} \, d\mathbf{x} - \int_{\Omega} \tilde{\mathbf{S}}^{n+1} \cdot \check{\mathbf{v}} \, d\mathbf{x}, \\
0 &= \int_{\Omega} \frac{\phi^{n+1} - \phi^n}{\tau} \check{\phi} \, d\mathbf{x} + \int_{\Omega} M\varepsilon \nabla \mu^{n+1} \cdot \nabla \check{\phi} \, d\mathbf{x} - \int_{\Omega} (\phi^n \mathbf{v}^{n+1}) \cdot \nabla \check{\phi} \, d\mathbf{x}, \\
0 &= \int_{\Omega} \mu^{n+1} \check{\mu} \, d\mathbf{x} - \int_{\Omega} \frac{W'_c(\phi^{n+1}) + W'_e(\phi^n)}{\varepsilon} \check{\mu} \, d\mathbf{x} - \int_{\Omega} \varepsilon \nabla \phi^{n+1} \cdot \nabla \check{\mu} \, d\mathbf{x}
\end{aligned} \tag{15}$$

holds for all $\check{p} \in \mathcal{V}_h^p$, $\check{\mathbf{v}} \in \mathcal{V}_h^v$ and $\check{\phi}, \check{\mu} \in \mathcal{V}_h^{\text{ch}}$ with

$$\int_{\Omega} \tilde{\mathbf{S}}^{n+1} \cdot \check{\mathbf{v}} \, d\mathbf{x} = - \int_{\Omega} \sigma(\phi^n \check{\mathbf{v}}) \cdot \nabla \mu^{n+1} \, d\mathbf{x}$$

and

$$\mathbf{J}_f^{n+1} = \rho \mathbf{J}^{n+1} = -\rho M\varepsilon \nabla \mu^{n+1}.$$

The terms $\tilde{\phi}_f^{n+1}$ and $\tilde{\rho}_f^{n+1}$ are to be understood as in their original definition, with all variables replaced by the finite element functions at time t_{n+1} , i.e., $\tilde{\phi}_f^{n+1} = 2\delta + (1 - 2\delta)\phi^{n+1}$ and $\tilde{\rho}_f^{n+1} = \rho(\phi^{n+1} + \delta)$.

We compose the discrete solution $(p_h, \mathbf{v}_h, \phi_h, \mu_h) : \Omega \times [0, T] \rightarrow \mathbb{R} \times \mathbb{R}^v \times \mathbb{R} \times \mathbb{R}$ through

$$(p_h, \mathbf{v}_h, \phi_h, \mu_h)(\mathbf{x}, t) = (p^n, \mathbf{v}^n, \phi^n, \mu^n)(\mathbf{x}, t) \quad (t \in [t^n, t^{n+1}]).$$

As for the weak solution we assume in what follows that the discrete solution $(p_h, \mathbf{v}_h, \phi_h, \mu_h)$ is uniquely determined and refer to [10] for analytical background.

4.2. Thermodynamic consistency of the fully-discrete solution

We now establish the discrete thermodynamic consistency by showing that the fully-discrete method satisfies an analog of the free energy dissipation inequality (8).

Theorem 4.1. *Assume that (15) can be solved by a function $(p_h, \mathbf{v}_h, \phi_h, \mu_h)(\cdot, t) \in \mathcal{V}_h^p \times \mathcal{V}_h^v \times \mathcal{V}_h^{\text{ch}} \times \mathcal{V}_h^{\text{ch}}$ for $t \in [0, T]$.*

Then, the discrete free energy dissipation inequality

$$\begin{aligned}
&\frac{1}{\tau} (F[\phi^{n+1}, \nabla \phi^{n+1}, \mathbf{v}^{n+1}] - F[\phi^n, \nabla \phi^n, \mathbf{v}^n]) \\
&\leq \int_{\Omega} -2\gamma \nabla^s \mathbf{v}^{n+1} : \nabla \mathbf{v}^{n+1} - \rho d(\tilde{\phi}_f^n, \varepsilon) |\mathbf{v}^{n+1}|^2 - \sigma M\varepsilon |\nabla \mu^{n+1}|^2 \, d\mathbf{x} \\
&\leq 0
\end{aligned} \tag{16}$$

is satisfied for all $n \in \{0, \dots, N_t - 1\}$, and hence

$$F[\phi^{n+1}, \nabla \phi^{n+1}, \mathbf{v}^{n+1}] \leq F[\phi^n, \nabla \phi^n, \mathbf{v}^n].$$

Proof. We test (15)₃ with $\check{\phi} = \sigma\mu^{n+1}$, yielding

$$0 = \int_{\Omega} \sigma \frac{\phi^{n+1} - \phi^n}{\tau} \mu^{n+1} d\mathbf{x} + \int_{\Omega} \sigma M\varepsilon |\nabla \mu^{n+1}|^2 d\mathbf{x} - \int_{\Omega} \sigma (\phi^n \mathbf{v}^{n+1}) \cdot \nabla \mu^{n+1} d\mathbf{x}, \quad (17)$$

and for $\check{\mu} = -\sigma(\phi^{n+1} - \phi^n)/\tau$ in (15)₄ we obtain

$$\begin{aligned} 0 = & - \int_{\Omega} \mu^{n+1} \sigma \frac{\phi^{n+1} - \phi^n}{\tau} d\mathbf{x} + \int_{\Omega} \frac{W'_c(\phi^{n+1}) + W'_e(\phi^n)}{\varepsilon} \sigma \frac{\phi^{n+1} - \phi^n}{\tau} d\mathbf{x} \\ & + \int_{\Omega} \varepsilon \nabla \phi^{n+1} \cdot \nabla \left(\sigma \frac{\phi^{n+1} - \phi^n}{\tau} \right) d\mathbf{x}. \end{aligned}$$

By the convexity of $W_c(\phi)$ and the concavity of $W_e(\phi)$ from (14) we have

$$W'_c(\phi^{n+1})(\phi^{n+1} - \phi^n) \geq W_c(\phi^{n+1}) - W_c(\phi^n) \quad \text{and} \quad W'_e(\phi^n)(\phi^{n+1} - \phi^n) \geq W_e(\phi^{n+1}) - W_e(\phi^n)$$

respectively, implying

$$(W'_c(\phi^{n+1}) + W'_e(\phi^n)) (\phi^{n+1} - \phi^n) \geq W_{\text{dw}}(\phi^{n+1}) - W_{\text{dw}}(\phi^n).$$

Hence, by the monotonicity of the integral we get

$$\int_{\Omega} \frac{W'_c(\phi^{n+1}) + W'_e(\phi^n)}{\varepsilon} \frac{\phi^{n+1} - \phi^n}{\tau} d\mathbf{x} \geq \int_{\Omega} \frac{1}{\tau} \frac{W_{\text{dw}}(\phi^{n+1}) - W_{\text{dw}}(\phi^n)}{\varepsilon} d\mathbf{x}.$$

Moreover, utilizing (A.2) we obtain

$$\int_{\Omega} \varepsilon \nabla \phi^{n+1} \cdot \frac{\nabla \phi^{n+1} - \nabla \phi^n}{\tau} d\mathbf{x} = \int_{\Omega} \frac{1}{\tau} \frac{\varepsilon}{2} |\nabla \phi^{n+1}|^2 d\mathbf{x} - \int_{\Omega} \frac{1}{\tau} \frac{\varepsilon}{2} |\nabla \phi^n|^2 d\mathbf{x} + \int_{\Omega} \frac{1}{\tau} \frac{\varepsilon}{2} |\nabla \phi^{n+1} - \nabla \phi^n|^2 d\mathbf{x}$$

and thus

$$\begin{aligned} 0 \geq & -\sigma \int_{\Omega} \frac{\phi^{n+1} - \phi^n}{\tau} \mu^{n+1} d\mathbf{x} + \sigma \left(\int_{\Omega} \frac{1}{\tau} \frac{W_{\text{dw}}(\phi^{n+1}) - W_{\text{dw}}(\phi^n)}{\varepsilon} d\mathbf{x} \right. \\ & \left. + \int_{\Omega} \frac{1}{\tau} \frac{\varepsilon}{2} |\nabla \phi^{n+1}|^2 d\mathbf{x} - \int_{\Omega} \frac{1}{\tau} \frac{\varepsilon}{2} |\nabla \phi^n|^2 d\mathbf{x} + \int_{\Omega} \frac{1}{\tau} \frac{\varepsilon}{2} |\nabla \phi^{n+1} - \nabla \phi^n|^2 d\mathbf{x} \right). \end{aligned} \quad (18)$$

Next, testing (15)₂ with $\check{\mathbf{v}} = \mathbf{v}^{n+1}$ yields

$$\begin{aligned} 0 = & \int_{\Omega} \frac{\tilde{\rho}_f^n + \tilde{\rho}_f^{n+1}}{2} \frac{\mathbf{v}^{n+1} - \mathbf{v}^n}{\tau} \cdot \mathbf{v}^{n+1} d\mathbf{x} \\ & + \frac{1}{2} \int_{\Omega} \left(\rho_f^n \mathbf{v}^{n+1} + \mathbf{J}_f^{n+1} \right) \cdot \nabla (\mathbf{v}^n \cdot \mathbf{v}^{n+1}) d\mathbf{x} \\ & - \int_{\Omega} p^{n+1} \nabla \cdot (\tilde{\phi}_f^{n+1} \mathbf{v}^{n+1}) d\mathbf{x} + \int_{\Omega} 2\gamma \nabla^s \mathbf{v}^{n+1} : \nabla \mathbf{v}^{n+1} d\mathbf{x} \\ & + \int_{\Omega} \rho d(\tilde{\phi}_f^n, \varepsilon) |\mathbf{v}^{n+1}|^2 d\mathbf{x} - \int_{\Omega} \tilde{\mathbf{S}}^{n+1} \cdot \mathbf{v}^{n+1} d\mathbf{x}. \end{aligned}$$

We have the algebraic relation

$$\begin{aligned} (\tilde{\rho}_f^n + \tilde{\rho}_f^{n+1})(\mathbf{v}^{n+1} - \mathbf{v}^n) \cdot \mathbf{v}^{n+1} &= \tilde{\rho}_f^{n+1} |\mathbf{v}^{n+1}|^2 - \tilde{\rho}_f^{n+1} \mathbf{v}^n \cdot \mathbf{v}^{n+1} + \tilde{\rho}_f^n |\mathbf{v}^{n+1} - \mathbf{v}^n|^2 + \tilde{\rho}_f^n \mathbf{v}^{n+1} \cdot \mathbf{v}^n - \tilde{\rho}_f^n |\mathbf{v}^n|^2 \\ &= \tilde{\rho}_f^{n+1} |\mathbf{v}^{n+1}|^2 - \tilde{\rho}_f^n |\mathbf{v}^n|^2 + \tilde{\rho}_f^n |\mathbf{v}^{n+1} - \mathbf{v}^n|^2 - (\tilde{\rho}_f^{n+1} - \tilde{\rho}_f^n) \mathbf{v}^n \cdot \mathbf{v}^{n+1} \end{aligned}$$

and hence

$$\begin{aligned} \int_{\Omega} \frac{\tilde{\rho}_f^n + \tilde{\rho}_f^{n+1}}{2} \frac{\mathbf{v}^{n+1} - \mathbf{v}^n}{\tau} \cdot \mathbf{v}^{n+1} d\mathbf{x} &= \int_{\Omega} \frac{1}{\tau} \frac{1}{2} \tilde{\rho}_f^{n+1} |\mathbf{v}^{n+1}|^2 d\mathbf{x} - \int_{\Omega} \frac{1}{\tau} \frac{1}{2} \tilde{\rho}_f^n |\mathbf{v}^n|^2 d\mathbf{x} \\ &\quad + \int_{\Omega} \frac{1}{\tau} \frac{1}{2} \tilde{\rho}_f^n |\mathbf{v}^{n+1} - \mathbf{v}^n|^2 d\mathbf{x} - \int_{\Omega} \frac{1}{2} \frac{\tilde{\rho}_f^{n+1} - \tilde{\rho}_f^n}{\tau} \mathbf{v}^n \cdot \mathbf{v}^{n+1} d\mathbf{x}. \end{aligned}$$

From testing (15)₁ with $\check{p} = p^{n+1}$, we thus obtain

$$\begin{aligned} 0 &= \int_{\Omega} \frac{1}{\tau} \frac{1}{2} \tilde{\rho}_f^{n+1} |\mathbf{v}^{n+1}|^2 d\mathbf{x} - \int_{\Omega} \frac{1}{\tau} \frac{1}{2} \tilde{\rho}_f^n |\mathbf{v}^n|^2 d\mathbf{x} + \int_{\Omega} \frac{1}{\tau} \frac{1}{2} \tilde{\rho}_f^n |\mathbf{v}^{n+1} - \mathbf{v}^n|^2 d\mathbf{x} - \int_{\Omega} \frac{1}{2} \frac{\tilde{\rho}_f^{n+1} - \tilde{\rho}_f^n}{\tau} \mathbf{v}^n \cdot \mathbf{v}^{n+1} d\mathbf{x} \\ &\quad + \frac{1}{2} \int_{\Omega} (\rho_f^n \mathbf{v}^{n+1} + \mathbf{J}_f^{n+1}) \cdot \nabla (\mathbf{v}^n \cdot \mathbf{v}^{n+1}) d\mathbf{x} + \int_{\Omega} 2\gamma \nabla^s \mathbf{v}^{n+1} : \nabla \mathbf{v}^{n+1} d\mathbf{x} \\ &\quad + \int_{\Omega} \rho d(\tilde{\phi}_f^n, \varepsilon) |\mathbf{v}^{n+1}|^2 d\mathbf{x} - \int_{\Omega} \tilde{\mathbf{S}}^{n+1} \cdot \mathbf{v}^{n+1} d\mathbf{x}. \end{aligned} \tag{19}$$

Note that by definition, see (3) we have $\tilde{\rho}_f^{n+1} - \tilde{\rho}_f^n = \rho_f^{n+1} + \rho\delta - (\rho_f^n + \rho\delta) = \rho(\phi^{n+1} - \phi^n)$ and therefore

$$\int_{\Omega} \frac{1}{2} \frac{\tilde{\rho}_f^{n+1} - \tilde{\rho}_f^n}{\tau} \mathbf{v}^n \cdot \mathbf{v}^{n+1} d\mathbf{x} = \int_{\Omega} \frac{1}{2} \rho \frac{\phi^{n+1} - \phi^n}{\tau} \mathbf{v}^n \cdot \mathbf{v}^{n+1} d\mathbf{x}.$$

Using $\check{\phi} = \frac{1}{2}\rho\mathbf{v}^n \cdot \mathbf{v}^{n+1}$ in (15)₃ yields

$$\begin{aligned} 0 &= \int_{\Omega} \frac{\phi^{n+1} - \phi^n}{\tau} \frac{1}{2} \rho \mathbf{v}^n \cdot \mathbf{v}^{n+1} d\mathbf{x} + \int_{\Omega} M\varepsilon \nabla \mu^{n+1} \cdot \nabla \left(\frac{1}{2} \rho \mathbf{v}^n \cdot \mathbf{v}^{n+1} \right) d\mathbf{x} \\ &\quad - \int_{\Omega} (\phi^n \mathbf{v}^{n+1}) \cdot \nabla \left(\frac{1}{2} \rho \mathbf{v}^n \cdot \mathbf{v}^{n+1} \right) d\mathbf{x} \\ &= \int_{\Omega} \frac{1}{2} \frac{\tilde{\rho}_f^{n+1} - \tilde{\rho}_f^n}{\tau} \mathbf{v}^n \cdot \mathbf{v}^{n+1} d\mathbf{x} - \frac{1}{2} \int_{\Omega} (\rho_f^n \mathbf{v}^{n+1} + \mathbf{J}_f^{n+1}) \cdot \nabla (\mathbf{v}^n \cdot \mathbf{v}^{n+1}) d\mathbf{x}, \end{aligned} \tag{20}$$

as $\rho_f^n = \rho\phi^n$ and $\mathbf{J}_f^{n+1} = -\rho M\varepsilon \nabla \mu^{n+1}$.

Finally, adding (17), (18), (19) and (20), and using that for the surface tension term we have

$$\int_{\Omega} \tilde{\mathbf{S}}^{n+1} \cdot \mathbf{v}^{n+1} d\mathbf{x} = - \int_{\Omega} \sigma(\phi^n \mathbf{v}^{n+1}) \cdot \nabla \mu^{n+1} d\mathbf{x},$$

we obtain

$$\begin{aligned} 0 &\geq \sigma \int_{\Omega} \frac{1}{\tau} \frac{W_{\text{dw}}(\phi^{n+1}) - W_{\text{dw}}(\phi^n)}{\varepsilon} d\mathbf{x} \\ &\quad + \sigma \left(\int_{\Omega} \frac{1}{\tau} \frac{\varepsilon}{2} |\nabla \phi^{n+1}|^2 d\mathbf{x} - \int_{\Omega} \frac{1}{\tau} \frac{\varepsilon}{2} |\nabla \phi^n|^2 d\mathbf{x} + \int_{\Omega} \frac{1}{\tau} \frac{\varepsilon}{2} |\nabla \phi^{n+1} - \nabla \phi^n|^2 d\mathbf{x} \right) \\ &\quad + \int_{\Omega} \frac{1}{\tau} \frac{1}{2} \tilde{\rho}_f^{n+1} |\mathbf{v}^{n+1}|^2 d\mathbf{x} - \int_{\Omega} \frac{1}{\tau} \frac{1}{2} \tilde{\rho}_f^n |\mathbf{v}^n|^2 d\mathbf{x} + \int_{\Omega} \frac{1}{\tau} \frac{1}{2} \tilde{\rho}_f^n |\mathbf{v}^{n+1} - \mathbf{v}^n|^2 d\mathbf{x} \\ &\quad + \int_{\Omega} \sigma M\varepsilon |\nabla \mu^{n+1}|^2 d\mathbf{x} + \int_{\Omega} 2\gamma \nabla^s \mathbf{v}^{n+1} : \nabla \mathbf{v}^{n+1} d\mathbf{x} + \int_{\Omega} \rho d(\tilde{\phi}_f^n, \varepsilon) |\mathbf{v}^{n+1}|^2 d\mathbf{x} \\ &= \frac{1}{\tau} (F[\phi^{n+1}, \nabla \phi^{n+1}, \mathbf{v}^{n+1}] - F[\phi^n, \nabla \phi^n, \mathbf{v}^n]) \\ &\quad + \int_{\Omega} \frac{1}{\tau} \sigma \frac{\varepsilon}{2} |\nabla \phi^{n+1} - \nabla \phi^n|^2 d\mathbf{x} + \int_{\Omega} \frac{1}{\tau} \frac{1}{2} \tilde{\rho}_f^n |\mathbf{v}^{n+1} - \mathbf{v}^n|^2 d\mathbf{x} \\ &\quad + \int_{\Omega} \sigma M\varepsilon |\nabla \mu^{n+1}|^2 d\mathbf{x} + \int_{\Omega} 2\gamma \nabla^s \mathbf{v}^{n+1} : \nabla \mathbf{v}^{n+1} d\mathbf{x} + \int_{\Omega} \rho d(\tilde{\phi}_f^n, \varepsilon) |\mathbf{v}^{n+1}|^2 d\mathbf{x} \end{aligned}$$

yielding the discrete free energy dissipation inequality

$$\begin{aligned} \frac{1}{\tau} (F[\phi^{n+1}, \nabla \phi^{n+1}, \mathbf{v}^{n+1}] - F[\phi^n, \nabla \phi^n, \mathbf{v}^n]) \\ \leq - \left(\int_{\Omega} \sigma M \varepsilon |\nabla \mu^{n+1}|^2 \, d\mathbf{x} + \int_{\Omega} 2\gamma \nabla^s \mathbf{v}^{n+1} : \nabla \mathbf{v}^{n+1} \, d\mathbf{x} + \int_{\Omega} \rho d(\tilde{\phi}_f^n, \varepsilon) |\mathbf{v}^{n+1}|^2 \, d\mathbf{x} \right) \leq 0 \end{aligned}$$

for all given τ and n . \square

5. Numerical solution strategies

In order to solve the discretized system of equations (15), we propose two schemes following the monolithic and partitioned solution paradigms, respectively.

5.1. Monolithic case

For the monolithic case we apply Newton's method in order to solve the coupled equations (15)_{1–4} collectively resolving the complex nonlinearities of the problem. Employing Newton's method requires the solution of linear systems with the Jacobian $\mathcal{A} \in \mathbb{R}^{N_m \times N_m}$ as system matrix. Here, the latter exhibits the general block structure

$$\mathcal{A} = \begin{pmatrix} A_{\text{CH}} & C_T \\ C_I & A_{\text{NS}} \end{pmatrix} \quad (21)$$

where $A_{\text{CH}} \in \mathbb{R}^{N_{\text{CH}} \times N_{\text{CH}}}$ denotes the Cahn-Hilliard block matrix, $A_{\text{NS}} \in \mathbb{R}^{N_{\text{NS}} \times N_{\text{NS}}}$ the Navier-Stokes block matrix, and $C_T \in \mathbb{R}^{N_{\text{CH}} \times N_{\text{NS}}}$ and $C_I \in \mathbb{R}^{N_{\text{NS}} \times N_{\text{CH}}}$ account for the coupling through the transport at the interface and the coupling through the interfacial force respectively, and hence $N_m = N_{\text{NS}} + N_{\text{CH}}$. In our implementation, the unknowns are ordered as $(\phi, \mu, \mathbf{v}, p)^T$ and the Cahn-Hilliard block refers to ϕ and μ while the Navier-Stokes block refers to \mathbf{v} and p . The matrix dimensions depend on the Lagrange finite element spaces used as discrete ansatz spaces. For the specific choice of $j = k = 1$, $l = 2$ in (13), that we employ in the numerical experiments in Section 7, we obtain the relation $N_{\text{NS}} \approx 4.5 \cdot N_{\text{CH}}$.

This approach directly addresses the interrelated dynamics of the coupled equations by taking into account the off-diagonal blocks of the Jacobian in each Newton iteration.

5.2. Partitioned case

For the partitioned case we decouple the system in the sense that we alternate in solving the Navier-Stokes equations (15)_{1,2} with operator A_{NS} and the Cahn-Hilliard equations (15)_{3,4} with operator A_{CH} with updated data from the other in an iterative loop, similar to the Strang splitting [33]. The resulting operator splitting has the advantage that problem-tailored solvers can be applied for the subsystems. Furthermore, for the fully coupled system there are also nonlinearities introduced in the coupling terms so that the splitting not only serves to decouple but also to partly linearize the system. However, it is clear that both subproblems remain highly nonlinear so that in order to solve them Newton's method is applied respectively.

This approach replaces the direct coupling by coupling iterations with smaller, potentially better conditioned Jacobians.

In Section 7.1.2 we assess both solution strategies in a comparative study for different flow regimes, which shows that both approaches are suitable for the solution of (15).

6. Generation of the initial condition ϕ_0

For a non-trivial initial phase distribution it is often more convenient to parametrize the sharp-interface formulation than to directly parametrize the required smooth phase field ϕ_0 . Here, we provide a two-step strategy to obtain ϕ_0 from arbitrary sharp-interface configurations. The formal workflow is as follows:

1. Choose an open set $\Phi \subset \Omega \subset \mathbb{R}^\nu$ representing the fluid phase. The sharp-interface configuration is then given by the characteristic function χ_Φ .
2. Do a small number of iterations n_{pre} of the Cahn-Hilliard operator A_{CH} alone with χ_Φ as initial condition and high mobility M_{pre} in order to obtain a diffuse-interface configuration ϕ_0 .

This strategy is especially useful in the partitioned setting as due to the underlying operator splitting the Cahn-Hilliard and Navier-Stokes operators are separately given, implemented and directly accessible.

Employing the strategy as a preprocessing step for the two-phase model enables us to calculate flow fields in complex geometries, see Section 7.2. To do so, the phase distribution should be almost static. We achieve this in practice by using a small mobility M for the Cahn-Hilliard operator after the preprocessing step.

Note that the switch of the mobility is key to obtain a valid strategy as the latter determines the time scale of the Cahn-Hilliard evolution. It is favorable to use a high preprocessing mobility M_{pre} in order for the diffuse profile to develop rapidly within only a small number of iterations n_{pre} of the Cahn-Hilliard operator. The parameters n_{pre} and M_{pre} are chosen due to numerical evidence. Conversely, for the actual flow calculations the time scale of interest is linked to the flow and hence the Cahn-Hilliard evolution should be comparably slow. Otherwise, this may, e.g., result in corners smoothing out over time further altering the complex geometry.

7. Numerical experiments

The numerical experiments presented here are divided mainly into three studies. Firstly, we investigate the thermodynamic consistency of the discrete numerical scheme, followed by a comparative study of the monolithic and partitioned strategies (cf. Section 5). To do so, we introduce a problem setup inspired by the classical fluid-flow problem of the lid-driven cavity extended to our two-phase model by adding circular solid inclusions in the flow. Furthermore, we want to assess the model's capability to capture flow scenarios in complex geometries following the strategy presented in Section 6. To do so, we introduce another problem setup that comprises a classical channel-flow setup extended by adding rectangular obstacles. Lastly, we extend model (1) to account for precipitation/dissolution effects at the liquid-solid interface and numerically investigate the extended model for an adapted channel-flow scenario. Before we present the simulations we collect some features of the numerical method.

Implementation details. The implementation is carried out in DUNE [34] and based on [35]. The latter builds on the finite element framework PDELab [36], which provides the usage of DUNE-ALUGrid [37] as a grid interface. All computations are carried out single-threaded on an AMD Ryzen Threadripper 2950X 16-Core Processor. In the following, we highlight some algorithmic features and parameters.

Spatial discretization and grid adaptivity. We use LBB-stable Taylor-Hood elements of degree $(2, 1)$ for the pair (\mathbf{v}, p) and piecewise linear Lagrange elements for ϕ and μ . Note that this corresponds to $j = k = 1$, $l = 2$ in (13).

As the diffuse transition zone of width $\mathcal{O}(\varepsilon)$ is small yet needs to be resolved properly, a resolution of the entire grid with finite elements of same size is computationally infeasible. Therefore, if not stated otherwise, we use grid adaptivity [37], where the simplicial mesh is refined based on the gradient of the phase-field variable ϕ [35, 3] leading to a fine resolution of the evolving transition layer.

Newton's method. We apply Newton's method from [36], where for the update step we employ the Hackbusch-Reusken line search [38]. Let m denote the iteration index of Newton's method and \mathbf{r}^m the corresponding residual vector. Newton's method is converged when the current residual reaches the stop tolerance maxTol defined as

$$\text{maxTol} = \max \left\{ \|\mathbf{r}^0\|_2 \text{relTol}, \text{absTol} \right\},$$

with relative tolerance relTol and absolute tolerance absTol . The linear solver tolerance linRed is set to

$$\text{linRed} = \max \left\{ \frac{\text{maxTol}}{10 \|\mathbf{r}^m\|_2}, \min \left\{ \text{minLinRed}, \frac{\|\mathbf{r}^m\|_2^2}{\|\mathbf{r}^{m-1}\|_2^2} \right\} \right\},$$

where minLinRed denotes the initial reduction parameter. We allow for a maximum number of m_N iterations. For the Hackbusch-Reusken line search we prescribe the maximum number of line search iterations m_{LS} and the damping factor d_{LS} .

Throughout all numerical experiments we set $m_N = 100$, $\text{relTol} = 10^{-7}$, $\text{absTol} = 10^{-9}$, $\text{minLinRed} = 10^{-3}$, $m_{\text{LS}} = 100$ and $d_{\text{LS}} = 0.5$. In case we solve the linear systems resulting from Newton's method directly, we use the direct solver UMFPack [39].

Double-well potential. Following Remark 2.1(i), the double-well potential is defined by

$$W_{\text{dw}}(\phi) = \phi^2(1 - \phi)^2 + \ell(\phi) + \ell(1 - \phi)$$

with limiter function ℓ . Here, we use

$$\ell(\phi) = \begin{cases} \delta_{\text{dw}} \left[\frac{\gamma_{\text{dw}}^2}{\delta_{\text{dw}} - \gamma_{\text{dw}}} + (\phi + \gamma_{\text{dw}}) \frac{-\gamma_{\text{dw}}(-\gamma_{\text{dw}} + 2\delta_{\text{dw}})}{(\delta_{\text{dw}} - \gamma_{\text{dw}})^2} \right] & \text{for } \phi \leq -\gamma_{\text{dw}} \\ \delta_{\text{dw}} \frac{\phi^2}{\phi + \delta_{\text{dw}}} & \text{for } -\gamma_{\text{dw}} < \phi < 0 \\ 0 & \text{for } \phi \geq 0 \end{cases} \quad (22)$$

with positive parameters $\delta_{\text{dw}} \leq \delta$ and γ_{dw} satisfying $0 < \delta_{\text{dw}} - \gamma_{\text{dw}} \ll 1$, and impose the convex-concave split as in [35]. Note that, in contrast to what is stated in Remark 2.1(i), the given limiter function $\ell(\phi)$ does not diverge at $\phi = -\delta$, and we apply this relaxation for stability reasons related to Newton's method. However, as long as the solution stays within $\phi > -\gamma_{\text{dw}}$, the solution is the same as for a limiter function that does not have the first case in (22) and would diverge at $\phi = -\delta_{\text{dw}}$.

Momentum dissipation in the solid phase. Remark 2.1(iii) states that in order to obtain a no-slip condition at the fluid-solid interface, we need to choose a sufficiently large momentum dissipation d_0 . However, for the standard drag term $d(\tilde{\phi}_f, \varepsilon) = d_0(1 - \tilde{\phi}_f)^2$ this may also lead to undesired velocity dissipation in the fluid for $\tilde{\phi}_f$ close to one. As remedy we utilize the modified drag term

$$d(\tilde{\phi}_f, \varepsilon) = \begin{cases} d_0 \frac{(d_{\text{max}} - \tilde{\phi}_f)^2}{d_{\text{max}}^2} & \text{for } \tilde{\phi}_f \leq d_{\text{max}} \\ 0 & \text{for } \tilde{\phi}_f > d_{\text{max}} \end{cases}$$

with constant dissipation cut-off $0 < d_{\text{max}} \leq 1$.

7.1. Lid-driven cavity inspired setup

We modify the classical lid-driven cavity setup known from fluid dynamics by incorporating circular solid inclusions in the fluid flow. Note that using the strategy presented in Section 6 is not needed here as a feasible (diffuse) initial profile ϕ_0 for the phase-field variable can directly be given. In order to do so, the corresponding parametrization describes a circle in terms of its center \mathbf{x}_c and its radius r , resulting in a radially symmetric formula for the spherical initial conditions. Energy considerations (for the Ginzburg-Landau energy) for the simple setting of a planar interface separating two phases result in a closed form expression of the one-dimensional equilibrium profile given by

$$\phi(x) = \frac{1}{2} \left(1 + \tanh \left(\frac{1}{\sqrt{2\varepsilon}} x \right) \right),$$

Table 1: Phase-field model parameters for the lid-driven cavity inspired setup. The given dimensions of the parameters are consistent with three spatial dimensions, where T, L and M denote the dimension symbols of time, length and mass respectively.

Parameter	Symbol	Value	Dimension
Fluid density	ρ	1.0	$L^{-3}M$
Fluid viscosity	γ	0.01	$T^{-1}L^{-1}M$
Momentum dissipation in solid phase	d_0	1000	T^{-1}
Dissipation cut-off	d_{\max}	0.9	—
Phase-field mobility	M	1.0	$T^{-1}L^2$
Surface tension coefficient	σ	1.0	$T^{-2}M$
Diffuse-interface width	ε	0.03	L
Phase-field regularization	δ	0.03	—
Double-well potential modification	δ_{dw}	0.02	—
Double-well potential modification	γ_{dw}	0.015	—

see e.g. [40, 41]. Extended to the radially symmetric case, for one circular inclusion the initial phase field then takes the form

$$\phi(\mathbf{x}, 0) = \frac{1}{2} \left(1 + \tanh \left(\frac{1}{\sqrt{2}\varepsilon} (\|\mathbf{x} - \mathbf{x}_c\|_2 - r) \right) \right).$$

In general, employing $N_s \in \mathbb{N}$ spheres in the flow field with parametrization

$$\phi_i(\mathbf{x}, 0) = \frac{1}{2} \left(1 + \tanh \left(\frac{1}{\sqrt{2}\varepsilon} (\|\mathbf{x} - \mathbf{x}_{i,c}\|_2 - r_i) \right) \right), \quad i \in \{1, \dots, N_s\},$$

the initial phase field takes the form

$$\phi(\mathbf{x}, 0) = \prod_{i=1}^{N_s} \phi_i(\mathbf{x}, 0).$$

For the velocity we utilize lid-driven cavity inspired Dirichlet boundary conditions, i.e., a parabolic velocity profile in horizontal direction on the top boundary of the domain $\Omega = [0, 2] \times [0, 1]$,

$$v_1((x_1, 1)^T, t) = \bar{f} \frac{2}{3} \frac{x_1(2 - x_1)}{2}, \quad t \in [0, T],$$

with mean flow \bar{f} , and value zero on the others. The velocity is initialized with value zero in the entire domain. For the phase field ϕ , chemical potential μ and pressure p we employ zero Neumann boundary conditions.

The phase-field model parameters are given in Table 1. Moreover, for the mean flow we set $\bar{f} = 0.1$.

7.1.1. Thermodynamic consistency

Due to the potential energy increase caused by coarsening of the computational grid [10], we do not enable grid adaptivity here during the simulation but only for the initial refinement step.

For the proof of thermodynamic consistency we have relied on the classical set of boundary conditions that comprises homogeneous Dirichlet conditions for the velocity \mathbf{v} . It is obvious that the latter is not satisfied for the lid-driven cavity inspired setup, where the flow boundary condition can be a source for an energy increase. Hence, in order to investigate the thermodynamic consistency for a non-trivial flow field, we use the following modification. In a preparatory step, we compute 30 time steps with the lid-driven cavity conditions. We then stop the driving flow to obtain a theoretically consistent initial flow field (and an equilibrated initial phase field) for the subsequent iterations of the two-phase model. The solid inclusion has center $\mathbf{x}_c = (0.5, 0.5)^T$ and radius $r = 0.2$. The resulting setup is depicted on the left of Figure 1. We

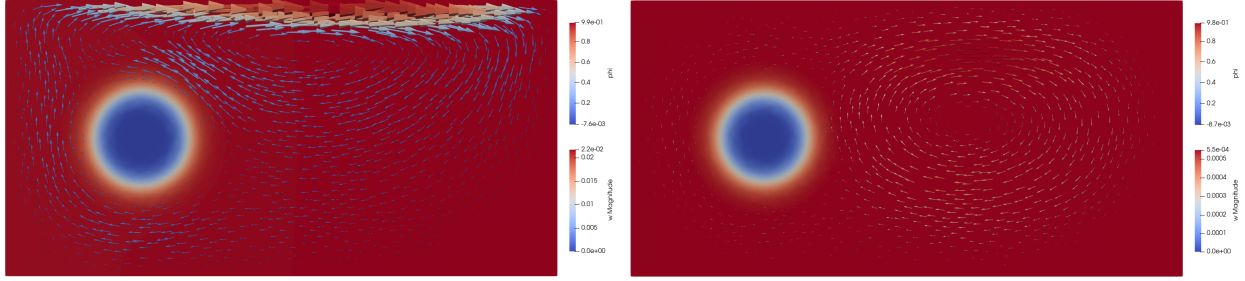


Figure 1: Lid-driven cavity inspired setup with one solid inclusion. On the left, we depict the result of the first time step after the inflow is stopped. On the right, we show the result of the final time step. The fluid phase is colored red and the solid phase blue. The phase transition is illustrated by the transition in color. The arrows are scaled according to the magnitude of the conserved quantity $\mathbf{w} := \tilde{\phi}_f \mathbf{v}$. The color scaling is due to the data ranges presented on the right of the respective subfigure. Note that the scaling is two orders of magnitude smaller in the right subfigure.

calculate a total of 200 time steps (comprising the preparatory ones) with time step size $\tau = 0.02$ resulting in final time $T = 4$ and the corresponding result is shown on the right of Figure 1.

For the parameters given, we find that the circular solid inclusion shrinks to some extent, while an inclusion with initial radius $r_v = 0.175$ vanishes completely. These observations comply with findings of [42] investigating spontaneous shrinkage of drops subject to Cahn-Hilliard diffusion. We note that the Cahn number for our setup is $Cn = \frac{\varepsilon}{r} = 0.15$. The volume of the domain Ω is $V = |\Omega| = 2$. The critical radius derived in [42] then evaluates to

$$r_c = \left(\frac{\sqrt{6}}{8\pi} V \varepsilon \right)^{\frac{1}{3}} = \left(\frac{3\sqrt{6}}{400\pi} \right)^{\frac{1}{3}} \approx 0.180,$$

i.e., for an initial radius $r < r_c$ the drop is predicted to vanish. Lastly, the formula for the shrinking of the drop radius presented in [42] evaluates to

$$\tilde{r} = -\frac{\sqrt{2}V}{24\pi} \frac{\varepsilon}{r^2} = -\frac{\sqrt{2}}{16\pi} \approx 0.028$$

and hence one obtains the reduced radius $r - \tilde{r} \approx 0.172$.

From these formulae, it is clear that there are measures to mitigate the shrinking process, such as decreasing ε , which may be taken given the implications on mass conservation discussed in [42]. Other possible adjustments comprise employing an adapted double-well potential [41] and reducing the mobility M to increase the shrinkage time (compared to the time scale of interest) [42]. We make use of the latter in our preprocessing strategy in Section 6.

In Figure 2 we depict the time evolution of the free energy (7) and the subenergies it is composed of, where we further split the Ginzburg-Landau energy into its two constituents. For the given setup, we observe that the Ginzburg-Landau energy for the Cahn-Hilliard evolution is orders of magnitude larger than the kinetic energy. Therefore, we scale the latter by a factor of 10^3 to properly show its curve in the plot. The dashed line marks the time step where we stop the inflow which is also reflected in the kinetic energy curve. The total energy is decreasing in accordance with Theorem 4.1.

7.1.2. Solution strategies

This section is devoted to assessing the monolithic and partitioned solution strategies of Section 5. We briefly discuss the blocks of the respective Jacobian matrices along with some matrix properties. Moreover, we introduce a feasible preconditioning technique for the partitioned case and conduct a comparative study with a focus on efficiency (in terms of runtime) and robustness (in terms of parameter variations).

For the comparative study, we establish three different solver setups; monolithic with direct solver, partitioned with both subsystems solved directly, and partitioned with tailor-made preconditioned iterative

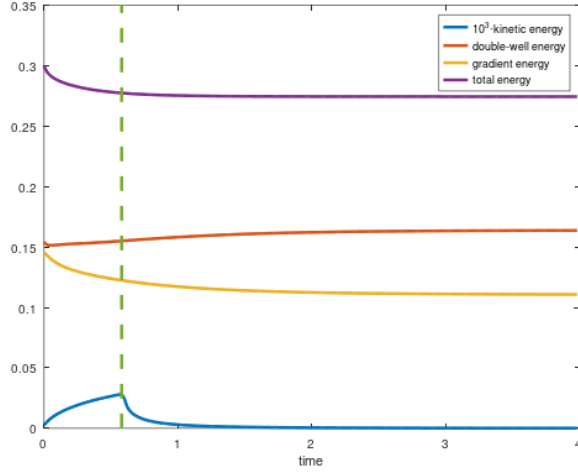


Figure 2: Energy plot for the lid-driven cavity inspired setup with one solid inclusion and stopped inflow (dashed line).

Table 2: 1-norm condition number estimates $\tilde{\kappa}$ for varying viscosity γ .

γ	10^{-4}	10^{-3}	10^{-2}	10^{-1}	1	10
$\tilde{\kappa}_{\mathcal{A}}$	$3.8 \cdot 10^{18}$	$6.6 \cdot 10^{18}$	$2.2 \cdot 10^{19}$	$7.3 \cdot 10^{19}$	$4.2 \cdot 10^{20}$	$1.5 \cdot 10^{21}$
$\tilde{\kappa}_{A_{NS}}$	$5.3 \cdot 10^{13}$	$9.9 \cdot 10^{11}$	$9.4 \cdot 10^{15}$	$2.5 \cdot 10^{18}$	$2.5 \cdot 10^{19}$	$1.5 \cdot 10^{21}$
$\tilde{\kappa}_{A_{CH}}$	1934.2	1934.2	1934.2	1934.2	1934.2	1934.2

solution. We again highlight that the underlying operator split in the partitioned setting leads to the iterative solution of the respective subsystems with matrices A_{CH} and A_{NS} , allowing the use of optimized subsystem solvers. It is thus clear that the last option offers various combinations and optimization potential, however, we merely focus on one specific choice to showcase the feasibility of the approach. As linear solver we employ Flexible Restarted GMRES (FGMRES) [43] for both subsystems, preconditioned with the ILU(0) preconditioner available in dune-istl [44] for Navier-Stokes and a SIMPLE-type preconditioner [45] for Cahn-Hilliard. The former is applicable to saddle-point problems where fill-in is produced mostly within the block of the factors corresponding to the (zero) pressure block. A brief discussion of the use of incomplete factorizations as preconditioners for saddle-point matrices is presented in [45]. We use a restart parameter of 200 for FGMRES with a maximum number of 1000 iterations for the Navier-Stokes and 10000 iterations for the Cahn-Hilliard solver.

We calculate 20 time steps with time step size $\tau = 0.02$ of the lid-driven cavity inspired setup with one solid inclusion. As a spatial measure we state the number of unknowns which intrinsically corresponds to the size of the solution vector of the linear system arising from Newton's method. For the initially refined grid, we denote the latter as N_m^0 for the monolithic scheme, and for the partitioned scheme we write N_{NS}^0 for the Navier-Stokes subsystem and N_{CH}^0 for the Cahn-Hilliard subsystem respectively. The computations show that over time there is a slight increase in the number of unknowns due to the adaptive grid refinement. To show that $N_* \in \mathcal{O}(N_*^0)$ still holds, we further state the numbers after the final refinement step N_*^f with $* \in \{m, NS, CH\}$.

We investigate the dependence of the monolithic and the partitioned matrix blocks and schemes based on the viscosity γ . As performance metrics we measure the CPU time. Note that for the partitioned scheme we start the iterative procedure by solving the Navier-Stokes subsystem first followed by the Cahn-Hilliard subsystem. In Table 2 we show 1-norm condition number estimates, calculated by invoking the command *condest* from GNU Octave, for the initial respective matrix blocks. Increasing the viscosity γ leads to an upward trend in the estimated condition numbers for both the monolithic matrix \mathcal{A} and the Navier-Stokes block A_{NS} , whereas the Cahn-Hilliard block A_{CH} does not depend on γ .

Table 3: Results for varying viscosity γ . For the reported CPU times, the symbol t(m) refers to the monolithic scheme, t(d) to the partitioned scheme with direct solution and t(i) to the partitioned scheme with iterative solution. ΣNi denotes the total number of Newton iterations and ΣCi the total number of coupling iterations. The cases where Newton's method did not converge are marked with “-”, and the number in brackets gives the corresponding time step. For the numbers of unknowns we have $N_m^0 = 22310$, $N_m^f = 23828$, $N_{CH}^0 = 4112$, $N_{CH}^f = 4388$, $N_{NS}^0 = 18198$ and $N_{NS}^f = 19440$.

γ	ΣNi	t (m)	ΣCi	ΣNi_{NS}	ΣNi_{CH}	t (d)	ΣCi	ΣNi_{NS}	ΣNi_{CH}	t (i)
10^{-4}	64	51.17	80	87	78	73.99	80	100	78	63.08
10^{-3}	60	48.64	80	92	78	77.30	80	100	78	63.65
10^{-2}	63	50.21	80	109	78	88.28	80	100	78	64.10
10^{-1}	80	64.43	80	157	78	121.88	80	102	80	77.01
1	(3)	—	—	(2)	—	—	80	110	88	114.41
10	(2)	—	—	(1)	—	—	82	119	95	149.69

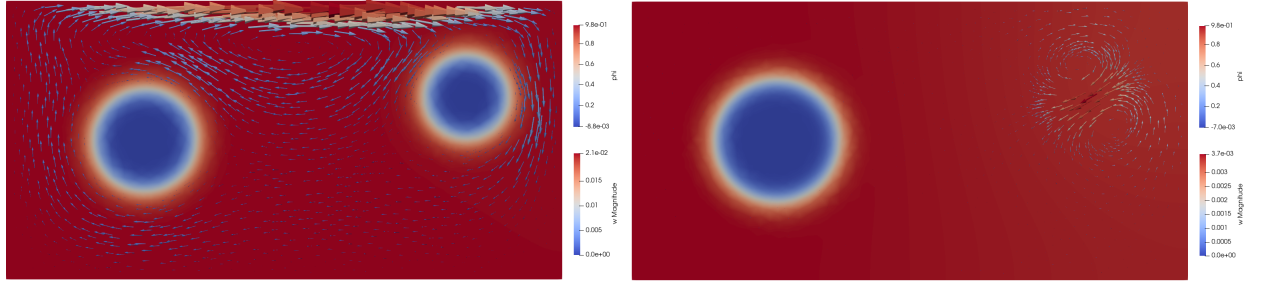


Figure 3: Lid-driven cavity inspired setup with two solid inclusions. On the left, we depict the result of the first time step after the inflow is stopped. On the right, we show the result of the time step where the smaller inclusion is completely vanished. The arrows are scaled according to the magnitude of the conserved quantity $w := \tilde{\phi}_f v$. The color scaling is due to the data ranges presented on the right of the respective subfigure, which is an order of magnitude smaller in the right subplot.

We show the results in Table 3. We highlight that the results reveal an increase in robustness for the fully iterative partitioned solution compared to the monolithic and partitioned schemes using solely the direct solver UMFPack. While these fail to converge for values $\gamma \geq 1$, the former converges for all viscosity values considered. Considering the range in which all schemes converge, we observe that the monolithic direct solver is the fastest. For the partitioned schemes, the iterative method is faster than its direct counterpart. The average number of coupling iterations per time step for the partitioned schemes to converge is (about) four. This indicates that the coupling terms C_T and C_I from (21) are rather weak which benefits the operator splitting.

The increase in robustness along with the high optimization potential related to the preconditioning strategies make the iterative partitioned scheme a preferred approach for the solution of the two-phase model.

7.1.3. Long-term model behavior

In order to investigate the long-term model behavior (and the related effect of the Cahn-Hilliard evolution), we propose the following experiment. We still use the lid-driven cavity inspired setup, but now with two (non-overlapping) solid inclusions with different radii. We keep the parameters from before including the solid inclusion with center $\mathbf{x}_{1,c} = (0.5, 0.5)^T$ and radius $r_1 = 0.2$. The second solid inclusion has its center in $\mathbf{x}_{2,c} = (1.65, 0.65)^T$ and radius $r_2 = 0.175 < r_1$. To assess the thermodynamic consistency, we again stop the inflow after 30 time steps. The resulting setup is depicted on the left of Figure 3.

We observe that the smaller inclusion is assimilated by the larger one as shown on the right of Figure 3, which is a well-known phenomenon of the Cahn-Hilliard evolution [40]. We now check the validity of the energy estimate in this rather involved setting. In Figure 4 we depict the time evolution of the free energy expression $F[\phi(\cdot, t), \nabla \phi(\cdot, t), \mathbf{v}(\cdot, t)]$ from (7) and its subenergies. For better illustration, we scale the kinetic energy by a factor of 10^4 , whose curve reflects the time step where the inflow is stopped, marked by the

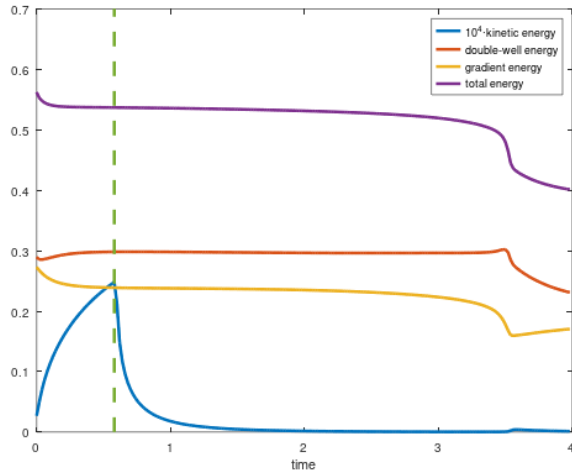


Figure 4: Energy plot for the lid-driven cavity inspired setup with two solid inclusions and stopped inflow (dashed line).

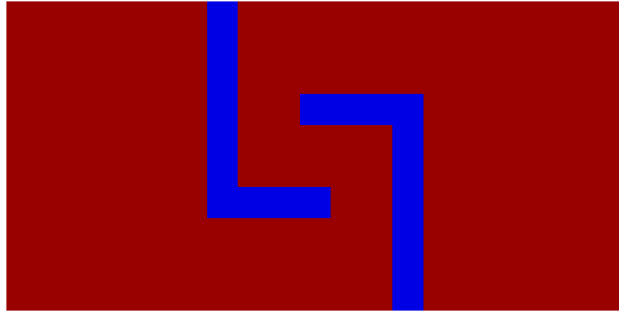


Figure 5: Sharp-interface configuration of the channel-flow inspired setup.

dashed line. The total energy is decreasing with a clearly observable drop at the time step when the smaller inclusion vanishes. This is due to the expected drop in the gradient energy in the instance of assimilation that is not compensated by the concomitant slight increase in the double-well and the kinetic energy.

7.2. Channel-flow inspired setup

We modify the classical channel-flow setup known from fluid dynamics by incorporating (overlapping) rectangular obstacles in the fluid flow with the governing scenario depicted in Figure 5. This non-trivial initial phase distribution can be parametrized in a sharp-interface formulation in a straightforward manner, which is not the case for the required diffuse-interface formulation. Hence, this model problem serves as a test case to assess the preprocessing strategy proposed in Section 6, where we generate a valid initial phase field ϕ_0 starting from a sharp-interface configuration of the initial phase distribution.

For the velocity we utilize Dirichlet boundary conditions comprising a parabolic velocity profile in horizontal direction on the left boundary (inflow) of the domain $\Omega = [0, 2] \times [0, 1]$,

$$v_1((0, x_2)^T, t) = \bar{f} \frac{2}{3} \frac{x_2(1 - x_2)}{4}, \quad t \in [0, T],$$

with mean flow \bar{f} , and value zero on the others. The velocity is initialized with zero value in the entire domain. For the pressure p we prescribe a fixed value $p_b = 0$ on the right boundary (outlet), and zero Neumann boundary conditions on the others. For the phase field ϕ we use Dirichlet boundary conditions on the left and right boundary to comply with the flow scenario and hence prescribe $\phi((0, x_2)^T, t) = 1 = \phi((2, x_2)^T, t)$.

Table 4: Phase-field model parameters for the channel-flow inspired setup. The given dimensions of the parameters are consistent with three spatial dimensions, where T, L and M denote the dimension symbols of time, length and mass respectively.

Parameter	Symbol	Value	Dimension
Fluid density	ρ	10^3	$L^{-3}M$
Fluid viscosity	γ	10^{-3}	$T^{-1}L^{-1}M$
Momentum dissipation in solid phase	d_0	10^3	T^{-1}
Dissipation cut-off	d_{\max}	0.9	—
Phase-field mobility	M	10^{-3}	$T^{-1}L^2$
Surface tension coefficient	σ	1.0	$T^{-2}M$
Diffuse-interface width	ε	$6 \cdot 10^{-3}$	L
Phase-field regularization	δ	$6 \cdot 10^{-3}$	—
Double-well potential modification	δ_{dw}	$4 \cdot 10^{-3}$	—
Double-well potential modification	γ_{dw}	$3 \cdot 10^{-3}$	—

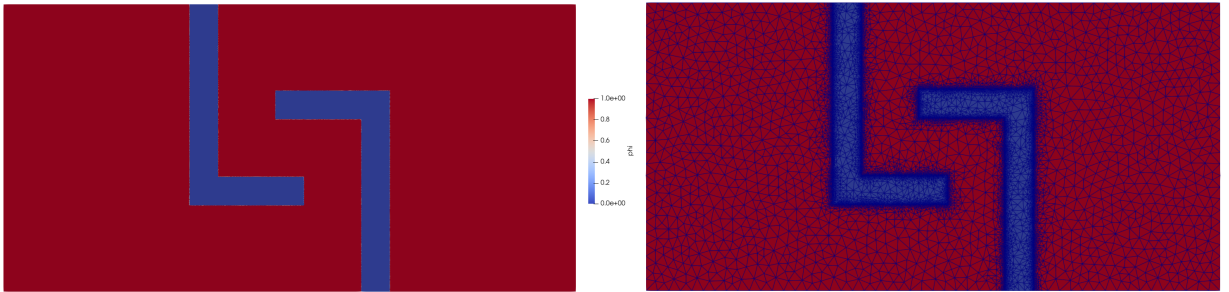


Figure 6: Sharp-interface configuration of the channel-flow inspired setup (left: implementation, right: refined grid).

For the bottom and top boundary, however, we use zero Neumann boundary conditions. Note that setting zero Neumann boundary conditions for ϕ on all boundaries may lead to a spurious emergence of the solid phase at the outlet over time (driven by the Cahn-Hilliard evolution). For the chemical potential μ we employ zero Neumann boundary conditions.

The phase-field model parameters are given in Table 4. Moreover, we set $\bar{f} = 0.1$ for the mean flow. For the second step of the preprocessing strategy introduced in Section 6, we employ $n_{\text{pre}} = 5$ iterations of the Cahn-Hilliard operator and set $M_{\text{pre}} = 10^3$ for the preprocessing mobility. In Figure 6 we show the initial profile gained from our implementation along with the refined computational grid. The refinement indicator is based on the gradient of the phase-field variable ϕ , so the grid refinement is applied predominantly in the interfacial region. In order to properly represent the sharp-interface configuration and to prevent spurious grid related effects a sufficiently high resolution of the interface is needed. In practice, we initially employ ten levels of refinement and we further refine the grid throughout the preprocessing strategy.

On the left of Figure 7 we depict the diffuse profile obtained after the first time step comprising the preprocessing step. We see that the preprocessing strategy (in combination with an appropriately refined grid) yields a good diffuse-interface representation of the profile in Figure 6. We calculate 200 time steps with time step size $\tau = 0.002$ resulting in final time $T = 0.4$. We depict the phase-field variable ϕ and the conserved quantity $\tilde{\phi}_f \mathbf{v}$ at the final time on the right of Figure 7. Firstly, we note that choosing a reasonably low mobility for the two-phase model evaluations we can satisfy the requirement of an almost static phase-field distribution. Secondly, the computed flow field shows the expected behavior of acceleration in the constriction built from the solid phase obstacles and deceleration afterwards.

These findings show the applicability of the two-phase model together with the preprocessing strategy for evaluating fluid flow in complex geometries.

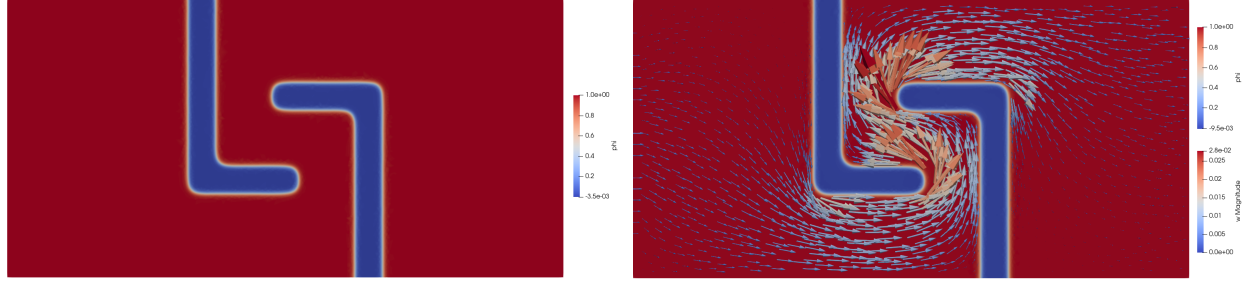


Figure 7: Diffuse-interface computation of the channel-flow inspired setup. We depict the result after the first time step on the left and the final one on the right. The arrows are scaled according to the magnitude of the conserved quantity $\mathbf{w} := \tilde{\phi}_f \mathbf{v}$. The color scaling is due to the data ranges presented on the right of the respective subfigure.

7.3. A Cahn-Hilliard Navier-Stokes model with precipitation/dissolution effects

In this section we consider an extension of model (1) to capture precipitation and dissolution of ions at the interface between the solid and the liquid as well as the motion of the ions in the fluidic phase. It coincides with the δ -2f1s-model presented in [2] for reactive transport with two fluidic phases in the reduced case of only one fluid phase present. For more work on precipitation/dissolution effects we refer to the recent work [46] using an Allen-Cahn Cahn-Hilliard ansatz and references therein.

7.3.1. Dynamics of a liquid-solid system with chemically reacting ion transport

First, we integrate terms for the chemical reaction process into our system (1). This leads with notations as in Section 2 and some reaction term R to

$$\begin{aligned} \nabla \cdot (\tilde{\phi}_f \mathbf{v}) &= 0, \\ \partial_t (\tilde{\phi}_f \mathbf{v}) + \nabla \cdot ((\rho_f \mathbf{v} + \mathbf{J}_f) \otimes \mathbf{v}) &= -\tilde{\phi}_f \nabla p + \nabla \cdot (2\gamma \nabla^s \mathbf{v}) - \rho d(\tilde{\phi}_f, \varepsilon) \mathbf{v} + \tilde{\mathbf{S}} + \frac{1}{2} \rho \mathbf{v} R, \\ \partial_t \phi + \nabla \cdot (\phi \mathbf{v} + \mathbf{J}) &= R, \\ \mu &= \frac{W'_{\text{dw}}(\phi)}{\varepsilon} - \varepsilon \Delta \phi \end{aligned} \quad \text{in } \Omega \times (0, T). \quad (23)$$

To account for the chemical effects, we add an evolution equation for the dissolved ion concentration $c = c(\mathbf{x}, t) \geq 0$. The equation is of convection-diffusion-reaction type and takes the form

$$\partial_t (\tilde{\phi}_c c) + \nabla \cdot ((\phi_c \mathbf{v} + \mathbf{J}_c) c) = D \nabla \cdot (\tilde{\phi}_c \nabla c) + R_c \quad (24)$$

with $\phi_c = \phi$, $\tilde{\phi}_c = \phi + \delta$, flux $\mathbf{J}_c = \mathbf{J}$, constant diffusivity D and reaction term R_c . The transport due to the Cahn-Hilliard equation is taken into account through the term $\nabla \cdot (\mathbf{J}_c c)$.

It remains to provide expressions for the reaction terms R and R_c . Following [2], the reaction terms R and R_c modeling ion precipitation and dissolution satisfy $R_c = c^* R$ with constant solid concentration c^* .

Before we present the numerical discretization for (23), (24) we reformulate (24) such that there is no reaction term in the concentration equation. In fact, the Cahn-Hilliard evolution (1)₃ is equivalent to

$$\partial_t \tilde{\phi}_c + \nabla \cdot (\phi_c \mathbf{v} + \mathbf{J}_c) = R.$$

Multiplying this with c^* and subtracting the result from (24), we obtain

$$\partial_t (\tilde{\phi}_c (c - c^*)) + \nabla \cdot ((\phi_c \mathbf{v} + \mathbf{J}_c) (c - c^*)) = D \nabla \cdot (\tilde{\phi}_c \nabla c).$$

For the weak formulation in terms of homogeneous Neumann boundary conditions on $\partial\Omega$ we have thus

$$0 = \int_{\Omega} \partial_t (\tilde{\phi}_c (c - c^*)) \check{c} \, d\mathbf{x} - \int_{\Omega} (c - c^*) \mathbf{J}_c \cdot \nabla \check{c} \, d\mathbf{x} - \int_{\Omega} \phi_c \mathbf{v} (c - c^*) \cdot \nabla \check{c} \, d\mathbf{x} + \int_{\Omega} D (\tilde{\phi}_c \nabla c) \cdot \nabla \check{c} \, d\mathbf{x}$$

Table 5: Concentration model parameters. The given dimensions of the parameters are consistent with three spatial dimensions, where T, L and N denote the dimension symbols of time, length and amount of substance respectively.

Parameter	Symbol	Value	Dimension
Diffusivity	D	1.0	$T^{-1}L^2$
Solid concentration	c^*	2.0	$L^{-3}N$
Reaction rate constant	k_c	0.1	$L^{-2}T^{-1}N$

for all $\check{c} \in H^1(\Omega)$.

Following a spatial discretization with first order Lagrange elements like in Section 4, we employ a semi-implicit Euler method in time to obtain the fully discrete version of the ion concentration equation by

$$0 = \int_{\Omega} \frac{\tilde{\phi}_c^{n+1}(c^{n+1} - c^*) - \tilde{\phi}_c^n(c^n - c^*)}{\tau} \check{c} \, d\mathbf{x} - \int_{\Omega} (c^{n+1} - c^*) \mathbf{J}_c^{n+1} \cdot \nabla \check{c} \, d\mathbf{x} \\ - \int_{\Omega} \phi_c^n \mathbf{v}^{n+1} (c^{n+1} - c^*) \cdot \nabla \check{c} \, d\mathbf{x} + \int_{\Omega} D(\tilde{\phi}_c^n \nabla c^{n+1}) \cdot \nabla \check{c} \, d\mathbf{x}$$

for all $\check{c} \in \mathcal{V}_h^{\text{ch}}$.

Moreover, the reaction term in (15)₂ and (15)₃ is discretized in a mixed way by

$$R^{n+1} = -\frac{q(\phi^n)}{\varepsilon} r(c^{n+1}), \quad (25)$$

where we choose $q(\phi) = \max\{\sqrt{2}\phi(1 - \phi), 0\}$ to localize the reaction to the fluid-solid interface. For the reaction rate we set $r(c) = k_c(c^2 - 1)$ which corresponds to a precipitation rate that increases with the ion concentration, a constant dissolution rate and an equilibrium concentration of $c_{\text{eq}} = 1$ [47]. k_c denotes the reaction rate constant. The semi-implicit discretization is chosen merely for numerical reasons as the nonlinearities in the coupling terms are now less pronounced and the resulting system is partly linearized. The Cahn-Hilliard Navier-Stokes system in (23) is discretized as in (15) using (25) for R . We have provided a discrete energy dissipation rate for (15) in Theorem 4.1. This question remains open for the reactive transport system. Nevertheless, our discretization works well also for this more complex system.

7.3.2. Precipitation/dissolution effects for a channel-flow setup

We consider a channel flow with the initial and boundary conditions from Section 7.2. Moreover, we initialize $c(\cdot, 0) = 1$ in the entire domain, and inject a fixed ion concentration of $c_b = 1.5$ at the inlet. On the other boundaries we set zero Neumann boundary conditions for c . We employ two circular solid inclusions in the flow with centers $\mathbf{x}_{1,c} = (0.5, 0.5)^T$ and $\mathbf{x}_{2,c} = (1.35, 0.65)^T$ and radius $r_1 = 0.2 = r_2$. The corresponding initial setup is depicted in the top left of Figure 8. The phase-field model parameters are the same as in Table 1 and the ones for the concentration are given in Table 5. We choose two solid inclusions of same radius in order to mitigate (geometric) effects of the Cahn-Hilliard evolution observed and discussed in the previous experiments and hence make the concentration related effects more pronounced. We calculate 300 time steps with time step size $\tau = 0.02$ resulting in final time $T = 6$.

The resulting phase-field distributions at different times are presented in Figure 8. As we inject a higher ion concentration, we expect net precipitation. This can be seen in the top right of Figure 8, where the solid inclusion closer to the inlet has grown. The inclusions coalesce (middle left), form a new bulk that grows further (middle right), reaches the top boundary (bottom left), and eventually also the bottom boundary (bottom right). Hence, we observe clogging and stop the simulation.

The distinct temporal evolution of the interfacial layer cannot be resolved without the use of adaptive grid refinement. As an impression of the dynamical change of the grid we show two grid instances in Figure 9.

8. Conclusions

We presented a fully-discrete finite element based method to solve the initial boundary value problem for an incompressible Cahn-Hilliard Navier-Stokes system that governs the evolution of a fluid-solid system

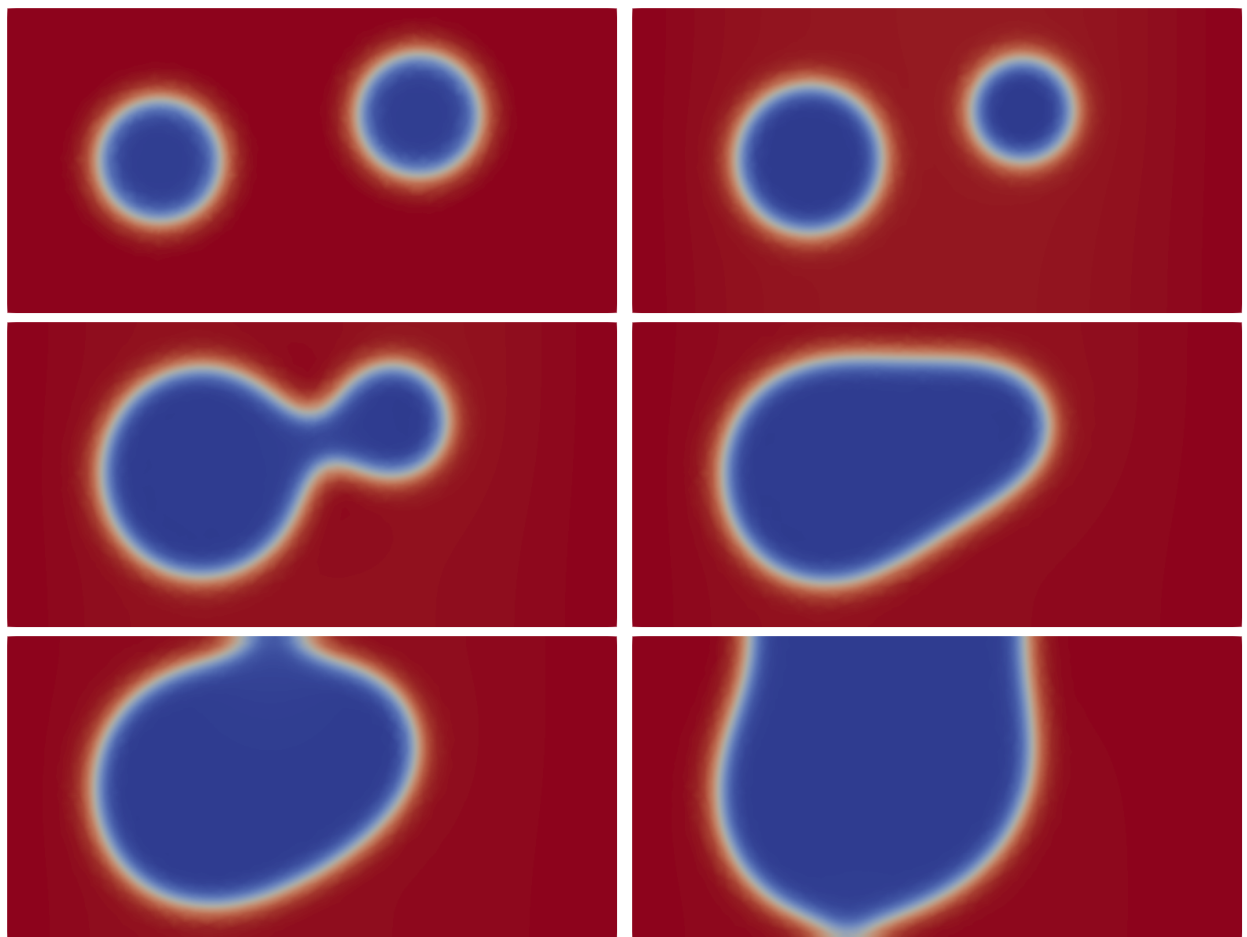


Figure 8: Phase-field variable ϕ at time $t \in \{0, 2, 3.36, 4, 4.5, 5.38\}$ (from top left to bottom right). The color scaling is based on the interval $\phi \in [-8.6 \cdot 10^{-3}, 1]$ limited by the extremal values found for these time steps.

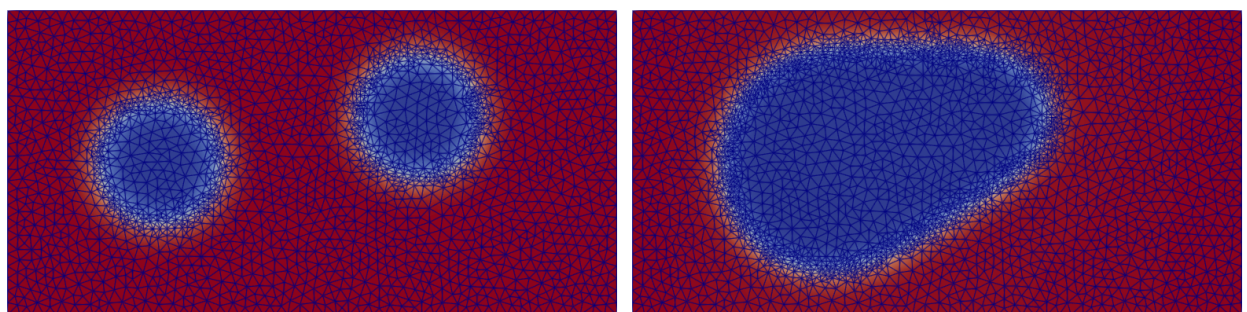


Figure 9: Refined grid at time $t \in \{0, 4\}$.

under geometric effects. We employed a tailor-made first-order time-stepping method that renders the fully-discrete approach to be unconditionally energy-stable. For the energy stability we exploited the convex-concave splitting of the non-convex free energy function and a tailored implicit-explicit discretization of the corresponding fluxes that allow to mimic the proof of the energy decay on the continuous level. We have shown the applicability of the method for a series of numerical experiments related to the lid-driven cavity problem and a channel-flow setup. A generalization of the method to a reactive flow problem with precipitation/dissolution demonstrates that our approach can handle also this more complex setup in a stable way.

Further research is devoted to finding higher-order in time methods to match the accuracy of the high-order space discretization. For a conditionally energy-stable second-order in time scheme which introduces time-step restrictions we refer to [48] whose scope is limited to the case of two fluid phases. The same applies for the use of discontinuous Galerkin methods. On the theoretical side it would be demanding to transfer Theorem 4.1 to flow systems that include transport of chemically reactive species.

Acknowledgement

Funded by Deutsche Forschungsgemeinschaft (DFG, German Research Foundation) under Germany's Excellence Strategy (Project Number 390740016 – EXC 2075) and the Collaborative Research Center 1313 (Project Number 327154368 – SFB 1313). We acknowledge the support by the Stuttgart Center for Simulation Science (SC SimTech).

Appendix A. Vector calculus

Lemma A.1. For (weakly) differentiable vector fields \mathbf{a} , \mathbf{b} and \mathbf{c} the identities

$$\nabla \cdot (\mathbf{a} \otimes \mathbf{b}) = (\nabla \cdot \mathbf{a})\mathbf{b} + (\mathbf{a} \cdot \nabla)\mathbf{b}, \quad \mathbf{b} \cdot ((\mathbf{a} \cdot \nabla)\mathbf{b}) = \frac{1}{2}(\mathbf{a} \cdot \nabla)|\mathbf{b}|^2, \quad (\text{A.1})$$

$$\mathbf{a} \cdot (\mathbf{a} - \mathbf{b}) = \frac{1}{2}|\mathbf{a}|^2 - \frac{1}{2}|\mathbf{b}|^2 + \frac{1}{2}|\mathbf{a} - \mathbf{b}|^2, \quad (\text{A.2})$$

$$((\mathbf{a} \cdot \nabla)\mathbf{b}) \cdot \mathbf{c} = \frac{1}{2}\mathbf{a} \cdot \nabla(\mathbf{b} \cdot \mathbf{c}) + \frac{1}{2}\mathbf{a} \cdot ((\nabla \mathbf{b})\mathbf{c}) - \frac{1}{2}\mathbf{a} \cdot ((\nabla \mathbf{c})\mathbf{b}) \quad (\text{A.3})$$

hold.

References

- [1] H. Abels, H. Garcke, G. Grün. Thermodynamically consistent, frame indifferent diffuse interface models for incompressible two-phase flows with different densities. *Math. Models Methods Appl. Sci.*, 22(03):1150013, 2012.
- [2] C. Rohde, L. von Wolff. A ternary Cahn–Hilliard–Navier–Stokes model for two-phase flow with precipitation and dissolution. *Math. Models Methods Appl. Sci.*, 31(01):1–35, 2021.
- [3] L. von Wolff. *The Phase Field Approach for Reactive Fluid–Solid Interfaces: Modeling and Homogenization*. Dissertation, University of Stuttgart, Hasselt University, 2023.
- [4] L. von Wolff, F. Weinhardt, H. Class, J. Hommel, C. Rohde. Investigation of Crystal Growth in Enzymatically Induced Calcite Precipitation by Micro-Fluidic Experimental Methods and Comparison with Mathematical Modeling. *Transp. Porous Media*, 137(2):327–343, 2021.
- [5] T. Schollenberger, L. von Wolff, C. Bringedal, I.S. Pop, C. Rohde, R. Helmig. Investigation of Different Throat Concepts for Precipitation Processes in Saturated Pore-Network Models. *Transp. Porous Media*, 151(14):2647–2692, 2024.
- [6] S. Aland. Time integration for diffuse interface models for two-phase flow. *J. Comput. Phys.*, 262:58–71, 2014.
- [7] G. Grün, F. Klingbeil. Two-phase flow with mass density contrast: Stable schemes for a thermodynamic consistent and frame-indifferent diffuse-interface model. *J. Comput. Phys.*, 257:708–725, 2014.
- [8] F. Guillén-González, G. Tierra. Splitting Schemes for a Navier–Stokes–Cahn–Hilliard Model for Two Fluids with Different Densities. *J. Comput. Math.*, 32(6):643–664, 2014.
- [9] J. Shen, X. Yang. Decoupled, Energy Stable Schemes for Phase-Field Models of Two-Phase Incompressible Flows. *SIAM J. Numer. Anal.*, 53(1):279–296, 2015.
- [10] H. Garcke, M. Hinze, C. Kahle. A stable and linear time discretization for a thermodynamically consistent model for two-phase incompressible flow. *Appl. Numer. Math.*, 99:151–171, 2016.

[11] G. Grün, F. Guillén-González, S. Metzger. On Fully Decoupled, Convergent Schemes for Diffuse Interface Models for Two-Phase Flow with General Mass Densities. *Commun. Comput. Phys.*, 19(5):1473–1502, 2016.

[12] A. Brunk, H. Egger, O. Habrich, M. Lukáčová-Medvid'ová. A second-order fully-balanced structure-preserving variational discretization scheme for the Cahn–Hilliard–Navier–Stokes system. *Math. Models Meth. Appl. Sci.*, 33(12):2587–2627, 2023.

[13] H. Bonart, C. Kahle, J.-U. Repke. Comparison of energy stable simulation of moving contact line problems using a thermodynamically consistent Cahn–Hilliard–Navier–Stokes model. *J. Comput. Phys.*, 399:108959, 2019.

[14] M. Shokrpour Roudbari, G. Şimşek, E.H. van Brummelen, K.G. van der Zee. Diffuse-interface two-phase flow models with different densities: A new quasi-incompressible form and a linear energy-stable method. *Math. Models Methods Appl. Sci.*, 28(04):733–770, 2018.

[15] Y. Palzhanov, A. Zhiliakov, A. Quaini, M. Olshanskii. A decoupled, stable, and linear FEM for a phase-field model of variable density two-phase incompressible surface flow. *Comput. Methods Appl. Mech. Eng.*, 387:114167, 2021.

[16] A. Giorgini, P. Knopf. Two-Phase Flows with Bulk–Surface Interaction: Thermodynamically Consistent Navier–Stokes–Cahn–Hilliard Models with Dynamic Boundary Conditions. *J. Math. Fluid Mech.*, 25(3):65, 2023.

[17] Z. Wang, H. Huang, P. Lin, S. Xu. A thermodynamically consistent phase-field model for mass transport with interfacial reaction and deformation. *arXiv preprint arXiv:2503.16765*, 2025.

[18] S. Minjeaud. An unconditionally stable uncoupled scheme for a triphasic Cahn–Hilliard/Navier–Stokes model. *Numer. Methods Partial Differ. Equ.*, 29(2):584–618, 2013.

[19] S. Aland, J. Lowengrub, A. Voigt. Two-phase flow in complex geometries: A diffuse domain approach. *Comput. Model. Eng. Sci.*, 57(1):77–108, 2010.

[20] Z. Guo, F. Yu, P. Lin, S. Wise, J. Lowengrub. A diffuse domain method for two-phase flows with large density ratio in complex geometries. *J. Fluid Mech.*, 907:A38, 2021.

[21] S.J. Ruuth, B. Merriman. Convolution–Thresholding Methods for Interface Motion. *J. Comput. Phys.*, 169(2):678–707, 2001.

[22] H. Chen, P. Dong, D. Wang, X.-P. Wang. A prediction-correction based iterative convolution-thresholding method for topology optimization of heat transfer problems. *J. Comput. Phys.*, 511:113119, 2024.

[23] H. Garcke, C. Hecht, M. Hinze, C. Kahle. Numerical Approximation of Phase Field Based Shape and Topology Optimization for Fluids. *SIAM J. Sci. Comput.*, 37(4):A1846–A1871, 2015.

[24] J. Bosch, C. Kahle, M. Stoll. Preconditioning of a Coupled Cahn–Hilliard–Navier–Stokes System. *Commun. Comput. Phys.*, 23(2):603–628, 2018.

[25] D. Kay, R. Welford. Efficient Numerical Solution of Cahn–Hilliard–Navier–Stokes Fluids in 2D. *SIAM J. Sci. Comput.*, 29(6):2241–2257, 2007.

[26] P. Çiloglu, C. Tretmans, R. Herzog, J.-F. Pietschmann, M. Stoll. Preconditioning for a Cahn–Hilliard–Navier–Stokes model for morphology formation in organic solar cells. *J. Comput. Phys.*, 540:114280, 2025.

[27] J.F. Blowey, C.M. Elliott. The Cahn–Hilliard gradient theory for phase separation with non-smooth free energy Part I: Mathematical analysis. *Eur. J. Appl. Math.*, 2(3):233–280, 1991.

[28] H. Brezis. *Functional Analysis, Sobolev Spaces and Partial Differential Equations*. Universitext. Springer, New York, 2011.

[29] H. Abels, D. Depner, H. Garcke. Existence of Weak Solutions for a Diffuse Interface Model for Two-Phase Flows of Incompressible Fluids with Different Densities. *J. Math. Fluid Mech.*, 15(3):453–480, 2013.

[30] P. Colli, S. Frigeri, M. Grasselli. Global existence of weak solutions to a nonlocal Cahn–Hilliard–Navier–Stokes system. *J. Math. Anal. Appl.*, 386(1):428–444, 2012.

[31] R. Verfürth. A posteriori error analysis of space-time finite element discretizations of the time-dependent Stokes equations. *Calcolo*, 47(3):149–167, 2010.

[32] D.J. Eyre. Unconditionally Gradient Stable Time Marching the Cahn–Hilliard Equation. *Mater. Res. Soc. Symp. Proc.*, 529:39–46, 1998.

[33] G. Strang. On the Construction and Comparison of Difference Schemes. *SIAM J. Numer. Anal.*, 5(3):506–517, 1968.

[34] O. Sander. *DUNE — The Distributed and Unified Numerics Environment*, volume 140 of *Lecture Notes in Computational Science and Engineering*. Springer Cham, 2020.

[35] L. von Wolff. The DUNE-Phasefield Module (release 1.0), 2021.

[36] P. Bastian, F. Heimann, S. Marnach. Generic implementation of finite element methods in the Distributed and Unified Numerics Environment (DUNE). *Kyberns.*, 46(2):294–315, 2010.

[37] M. Alkämper, A. Dedner, R. Klöfkorn, M. Nolte. The DUNE-ALUGrid Module. *Arch. Numer. Softw.*, 4(1):1–28, 2016.

[38] W. Hackbusch, A. Reusken. Analysis of a damped nonlinear multilevel method. *Numer. Math.*, 55(2):225–246, 1989.

[39] T.A. Davis. Algorithm 832: UMFPACK V4.3—an unsymmetric-pattern multifrontal method. *ACM Trans. Math. Softw.*, 30(2):196–199, 2004.

[40] C. Liu, J. Shen. A phase field model for the mixture of two incompressible fluids and its approximation by a Fourier-spectral method. *Phys. D: Nonlinear Phenom.*, 179(3):211–228, 2003.

[41] A.A. Donaldson, D.M. Kirpalani, A. Macchi. Diffuse interface tracking of immiscible fluids: Improving phase continuity through free energy density selection. *Int. J. Multiph. Flow*, 37(7):777–787, 2011.

[42] P. Yue, C. Zhou, J.J. Feng. Spontaneous shrinkage of drops and mass conservation in phase-field simulations. *J. Comput. Phys.*, 223(1):1–9, 2007.

[43] Y. Saad. *Iterative Methods for Sparse Linear Systems*. Society for Industrial and Applied Mathematics, second edition, 2003.

[44] M. Blatt, P. Bastian. The Iterative Solver Template Library. In B. Kågström, E. Elmroth, J. Dongarra, J. Waśniewski,

editor, *Applied Parallel Computing. State of the Art in Scientific Computing*, volume 4699 of *Lecture Notes in Computer Science*, pages 666–675, Berlin, Heidelberg, 2007. Springer Berlin Heidelberg.

- [45] M. Benzi, G.H. Golub, J. Liesen. Numerical solution of saddle point problems. *Acta Numer.*, 14:1–137, 2005.
- [46] A. Lamperti, L. De Lorenzis. A variationally consistent and asymptotically convergent phase-field model for solute precipitation and dissolution. *J. Comput. Phys.*, page 114665, 2026.
- [47] C. Bringedal, L. von Wolff, I.S. Pop. Phase Field Modeling of Precipitation and Dissolution Processes in Porous Media: Upscaling and Numerical Experiments. *Multiscale Model. Simul.*, 18(2):1076–1112, 2020.
- [48] M.A. Khanwale, K. Saurabh, M. Fernando, V.M. Calo, H. Sundar, J.A. Rossmanith, B. Ganapathysubramanian. A fully-coupled framework for solving Cahn-Hilliard Navier-Stokes equations: Second-order, energy-stable numerical methods on adaptive octree based meshes. *Comput. Phys. Commun.*, 280:108501, 2022.